Restructuring in high burn-up UO_2 fuels: experimental characterization by electron backscattered diffraction

Isabelle Zacharie-Aubrun[1], Rebecca Dowek[1,2], Jean Noirot[1], Thierry Blay[1], Martiane Cabié[3], Myriam Dumont[4]

[1] *CEA, DES, IRESNE, DEC, Cadarache F-13108 Saint-Paul-Lez-Durance, France, isabelle.aubrun@cea.fr*
[2] *Aix-Marseille University, Institut Matériaux Microélectronique Nanosciences de Provence-IM2NP, UMR CNRS 7334, France*
[3] *Aix Marseille Univ., CNRS, FSCM, CP2M, France*
[4] *Arts et Métiers Institute of Technology, MSMP, HESAM Université, F-59000 Lille, France*

ABSTRACT

This paper discusses the use of electron back-scattered diffraction to characterize restructuring in a set of UO_2 samples, irradiated in a pressurized water reactor at a burn-up between 35 and 73 GWd/t_U, including standard UO_2 samples and Cr-doped UO_2 samples, to provide a better understanding of restructuring occurring both on the periphery and in the center of high-burn-up pellets. The formation of a high burn-up structure on the periphery of high burn-up UO_2 was confirmed in our experiment. We found restructuring associated with bubble formation of all the samples in the central area, with higher irradiation temperatures when the burn-up exceeded 61 GWd/t_U, regardless of their initial microstructure. This restructuring tended to progress with the increasing burn-up and to sub-divide the initial grains into sub-grains, with orientations close to that of the parent grains. Radial changes and differences between these samples showed that the burn-up and the temperature were not the only relevant parameters involved in restructuring.

1 INTRODUCTION

The formation of a high burn-up structure (HBS), on the rim of high burn-up light water reactor (LWR) UO_2 fuel pellets, in Pu rich areas of heterogeneous MOX fuels and on the periphery of fast reactor (FR) fuels, has been explored in many papers using various and complementary approaches[1,2,3,4,5,6,7,8,9,10,11,12,13]. A review was also written by Rondinella and Wiss in 2010[14]. However, only a few experiments have used electron back-scattered diffraction (EBSD) to study this phenomenon. This is mainly because only a few hot laboratories have access to such a device for irradiated fuel studies on LWR (Bengstsson et al.[15], Jädernäs et al.[16], Gerczak et al.[17], Noirot et al.[18], Cappia et al.[19]) and on FR (Teague et al.[20], Frazer et al.[21]). In the same burn-up range in which HBS forms on the rim of the LWR UO_2 fuel pellets, micrometric or sub-micrometric fission gas bubbles form in the central area of the pellets. This phenomenon is generally attributed to the combined effect of the highest temperatures and the increasing fission gas build-up, it has not been studied as much as the HBS phenomenon. Noirot et al.[22] showed that, in these central areas, the grain contrasts due to electron channeling differences in scanning electron microscopy (SEM) images did not allow for grain separation in sample preparations where this was possible outside the central area. In Noirot et al.[13], it was not easy to identify the grain boundaries (GB) in the center of a 73 GWd/t_U SEM fractography, and the bubbles were neither spherical (as typical intragranular bubbles) nor clearly lenticular (as typical intergranular bubbles). They did not seem to be widely interconnected either. The first questions raised by these observations were addressed by Noirot et al.[18] combining 3D focused ion beam (FIB) coupled with scanning electron microscope (SEM) examinations and EBSD on the same 73 GWd/t_U fuel. These techniques showed the formation of low-angle boundary sub-domains, called sub-grains in this article, within the initial grains. These sub-grains had crystal orientations close to those of

their respective parent grains. These examinations also showed the presence of bubbles with complex shapes, located on sub-grain boundaries, and the absence of an interconnected bubble network.

Within the framework of PhD research by R. Dowek[23], this new study applied the EBSD technique to a set of samples with a wider range of burn-ups (35-73 GWd/t_U), including both UO_2 and chromium-doped UO_2 samples with larger grains. The first part of this article provides a brief review of previous studies on high burn-up fuels using an EBSD device. The second part describes the characteristics of the irradiated fuel samples and the EBSD measurements chosen to analyze the microstructure of these samples. In the third part, the radial microstructure changes with the burn-up are described based on the EBSD results. The last section of this paper discusses restructuring on the periphery and in the central area of the fuel samples. A companion article exposes the results of the 3D FIB-SEM examination technique to explore the variations in the bubble population and their shapes, applied to the same high burn-up samples (Noirot et al.[24]).

2 PREVIOUS EBSD STUDIES ON HIGH BURN-UP LWR FUELS

In 1996 (Bengstsson et al.[15]), EBSD applied on the periphery of a 65 GWd/t_U sample revealed the complete restructuring into HBS with a sub-division into sub-micrometer grains, with many micrometric bubbles on the rim of the pellet and random small new grain orientations. It also showed partial restructuring at 340 µm from the pellet periphery, into sub-grains mainly near the parent grain boundaries. This work equally highlighted a number of increased misorientations around the parent grain orientation in the still unrestructured parts of the grains.

Jädernäs et al.[16] studied standard UO_2, Al-Si-doped and Al-Cr-doped UO_2 pellets with local section burn-ups between 48 and 56 GWd/t_U, ramped up to local linear powers of 300 to 400 W/cm. They used EBSD and FIB-SEM before and after the ramp tests. These studies showed the formation of low-angle boundary sub-grains in the center of the doped fuel pellets prior to the ramp-ups. The sub-grain diameters were typically below 1 µm. The bubbles appeared preferentially on the sub-grain boundaries. They also showed early stages of HBS formation on the rim, with differences that were considered to be qualitatively consistent with sample burn-up differences. It was noted that HBS sub-grains in these early stages of HBS formation showed both low- and high-angle boundaries. In these examinations, the HBS was found to begin inside the grains and to progress towards the grain boundaries.

The study by Gerczak et al.[17] provides detailed EBSD examinations on a high burn-up irradiated UO_2 sample. In this work, a short longitudinal section of a UO_2 fuel sample, covering ~0.25R – 1R (where R is the pellet's radius, 1R its periphery and 0R its center – convention that will be used all through this article) was examined using EBSD, SEM 2D, transmission Kikuchi diffraction (tKD), and scanning transmission electron microscopy (STEM) with energy dispersive X-ray spectroscopy (EDS). The fuel was a 2.9% ^{235}U fuel pellet with a diameter of 9.06 mm before irradiation. This fuel was irradiated in the H.B. Robinson Unit 2 pressurized water reactor, as part of an experimental program. The linear power for the central region of the rod showed a general decrease from ~260 W/cm to ~120 W/cm. The rod fission gas release at the end of the irradiation was 2.1% of the production. The specimen burn-up was 72 GWd/t_U. The sample also exhibited the formation of low-angle boundary sub-grains within the parent grains in the central area, similarly to what had been shown in Noirot et al.[18]. It has been used for comparison with our new results.

More recently, Cappia et al.[19] published a post-irradiation characterization of a pressurized water reactor (PWR) fuel at high burn-up (76 GWd/tM) at different scales, by optical microscopy, EPMA, SEM, EBSD and TEM. The rod fission gas release at the end of the irradiation was 16% of the production. Three different zones in the pellet were studied: a central area (0R-0.55R), an intermediate zone (0.55R – 0.75R), and the rim zone. In this paper, EBSD maps were acquired to provide a qualitative analysis of the grain structure. The sub-division of the parent grains, in the central area, due to low-angle grain boundaries (LAGB),

abruptly stopped in the intermediate zone. There was also an increase in the size of the LAGB from the center to the mid radius. The recrystallized HBS grains in the rim zone were free of dislocations network.

3 SAMPLES AND EXAMINATION DEVICES

The specimens studied by EBSD and used in this work were all PWR irradiated UO_2 fuel cross sections, embedded in a low melting point Sn-Bi alloy under vacuum. Their surface was mechanically ground with SiC papers and polished with diamond suspensions down to 0.25 µm grade, with a final step using a colloidal suspension of silica with a particle size of 0.02 µm.

The main features of the fuels (e.g. fabrication characteristics and burn-ups) are summarized in Table 1. These samples cover a range of burn-ups, from intermediate burn-ups, prior to the HBS formation and clear central precipitation of fission gases, to high burn-ups. Standard UO_2 (Std) fuels were examined as well as Cr-doped UO_2 (Cr) fuels where the dopant was added to promote the formation of large grains during the pellet sintering. The labels used, herein to name these specimens combine the type of fuel (Std or Cr) and its burn-up expressed in GWd/t_U (35 to 73). Standard unirradiated UO_2 specimens were also used for reference purposes.

Table 1: Characteristics of the studied samples

Label	Fuel	Axial height (mm/bottom rod)	Burn-up (GWd/t_U)		Grain size (µm)	^{235}U (%)	Pellet Ø (mm)	Porosity (%)	FGR (%)
			rod	specimen					
Std-36	Standard UO_2	3786	37.3	36.1	9.1	4.95	8.192	4.85	0.53
Std-61	Standard UO_2	1321	56.7	61.4	8.8	4.48	8.193	3.95	2.75
Std-63	Standard UO_2	3812	65.1	63.5	9.1	4.95	8.192	4.85	4.30
Std-73	Standard UO_2	2970	67.5	72.7	10.3	4.49	8.086	4.69	6.17
Cr-35	Cr doped UO_2	3682	33.8	35.4	56.5	4.49	8.193	3.14	0.23
Cr-63	Cr doped UO_2	3783	63.7	62.7	60.1 but smaller on periphery	4.89	8.192	2.80	3.04

The porosity of the fresh fuels, evaluated using apparent density measurements by immersion, was between 2.8% and 4.9%. The initial ^{235}U enrichment was between 4.5% and 5%. The added Cr_2O_3 doping in the Cr-doped UO_2 fuels was 0.16 wt%. The grain size of the standard UO_2 was around 10 µm. The grain size for the Cr-doped UO_2 was larger at around 60 µm, except on the periphery where the grain size was between 20 and 40 µm, as measured by a mean linear intercept method[25]. The different rods underwent non destructive examinations, such as gamma scanning. They were then punctured to measure the fission gas release (FGR) fractions. The FGR measurements showed a general increase with the rod burn-up. When compared to the specimen used in Gerczak et al.[17], the fuel enrichments were higher (4.5 to 5%, for the high burn-ups instead of 2.9%), the pellet diameters were smaller (8.09 to 8.19 mm instead of 9.06 mm) and the fission gas release fractions were higher.

Fig.1 shows the simplified linear power histories as a function of the irradiation time, at the axial elevation of the specimens studied. It also gives the resulting temperature histories along the rod centerlines for this same level, as calculated by the Alcyone fuel behavior code[26,27]. Apart from the Std-73 sample, the average power of all the high burn-up specimens decreased over time and fell in the range of 120 to 162 W/cm during their last cycle. The standard UO_2 sample with the highest burn-up (Std-73) underwent a linear power history where the second irradiation cycle was at low power (around 86 W/cm) but its sixth annual cycle had a long period of around 190 W/cm, and a final cycle of around 120 W/cm. Std-61 sample had the highest linear powers, i.e. between 200 and 250 W/cm, during its three first annual cycles, although its last cycle that was around 158 W/cm. Samples Std-36, Std-63, and Cr-63 were cut at axial levels where the local average section burn-up was lower than the rod average burn-up, whereas Std-61,

Std-73 and Cr-35, were from the high burn-up parts of their rods. The axial heights of the samples are given from the bottom of the rod as shown in Table 1.
The axial Std-73 and Std-61 samples were irradiated in reactors with refueling cycles of 12 months, or18 months for the other specimens.

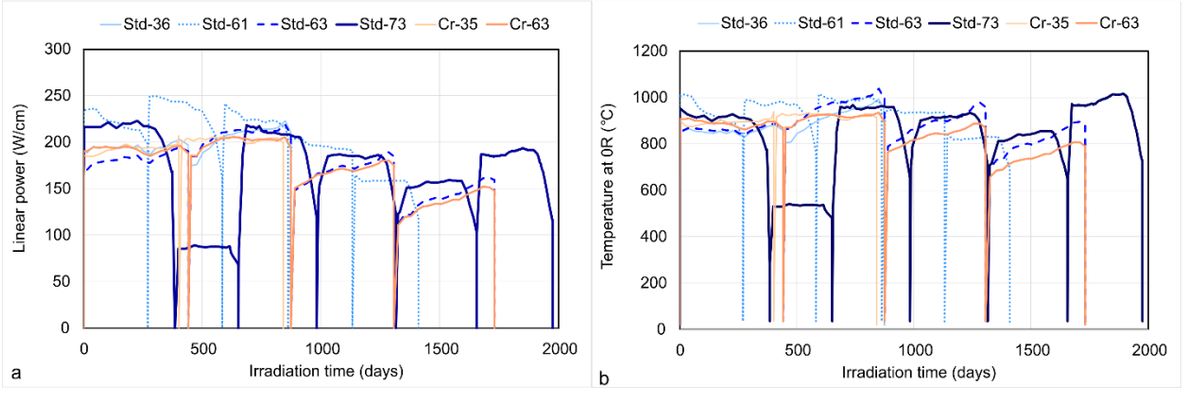

Fig.1. (a) simplified linear power, (b) centerline temperature histories, at the specimen levels (Alcyone code calculations).

We considered three main zones in the high burn-up samples, namely the central area, the intermediate zone, and the rim, where HBS is formed. The transition from the intermediate zone to the rim is progressive, and is called the HBS transition zone. This is illustrated in Fig.2 which shows the radial profile of xenon (Xe) as measured by electron probe microanalysis (EPMA) on the Std-61 sample. Xe measurements in the central area are low when compared to the local production of Xe because of the partial gas release during irradiation in reactor and the presence of practically micrometric fission gas bubbles, releasing their gas when cut during sample polishing. Xe measurements in the intermediate zone are close to the local Xe production. Xe measurements on the HBS rim are low because of high burn-up structure (HBS) formation with a sub-division into sub-micrometer grains and many micrometric bubbles and gas bubbles opening during sample polishing. The partial formation of HBS in the HBS transition zone, gradually increases towards the rim zone.

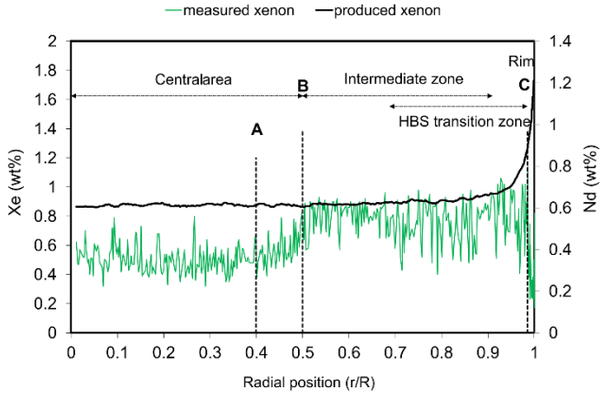

Fig.2. Std-61: EPMA xenon profiles of the measured xenon and the produced xenon determined using the neodymium profile.

Table 2 gives the limits of the central area (A and B) and the rim zone (C), determined using the EPMA xenon profiles of each high burn-up irradiated studied sample.
SIMS xenon profiles were also obtained to help determine the amount of FG in the bubbles, as shown for the Std-73 in Noirot et al.[13]. Almost all of the FG produced were measured by SIMS from the intermediate zone to the periphery of the pellet. FG were likely missed in the hottest zone of the central area.

Table 2. Central area and periphery zone limits (rim) for the samples determined using xenon radial profiles measured by EPMA.

Label	Central area		Rim zone
	A	B	C
Std-36			
Std-61	0.40 R	0.50 R	0.985 R (58 µm)
Std-63	0.37 R	0.43 R	variable (~40 à 80 µm)
Std-73	0.24 R	0.40 R	~0.98 R(~80 µm)
Cr-35			
Cr-63	0.15 R	0.35 R	0.98 R (80 µm)

The FIB-SEM Auriga 40 (Carl Zeiss, Oberkochen, Germany) used for this work, is located in the CEA Cadarache LECA-STAR hot-cell facility. The device is housed in a shielded cell and is connected to a glove box to prevent contamination[28,29].

EBSD maps were acquired with a Nordlys camera (maximum CCD resolution 1344x1024) at an acceleration voltage of 20 kV, a current of 2 nA in high current mode and at a working distance of ~17 mm. The samples were tilted at 70°. The Kikuchi patterns were indexed with Aztec software (Oxford Instruments, Abington-on-Thames, UK) in the "refined accuracy" mode with the Fm3m space group 225 for the fluorite-structured UO_2. EBSD camera settings were 2x2 binning (CCD resolution 672x512 pixels). The maps were corrected to remove the indexed pixels in the pores and to reduce noise according to the method explained in ref of Ben Saada[30]. Orientation maps, in inverse pole figure (IPFZ) were built with a color code defined in Fig.3 that gives the direction of the crystal parallel to the normal to the sample surface, for cubic symmetry. The minimum misorientation of detection for a boundary that does not take into account noise and that highlights maximum restructuring and sub-grain formation, is 1°.

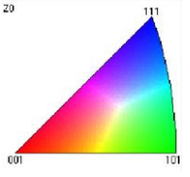

Fig.3. Color coding in the EBSD Inverse pole figure map (IPFZ).

The examinations started in 2016 when the FIB-SEM was first used on irradiated fuels and they continued through to 2022. This explains why the acquisition methodology for this set of results had not yet been stabilized and evolved from one sample to the other. This is mainly visible in the differences in the field sizes and in the scanning steps used for these examinations. The usual contradictive needs for large fields were taken into account; large fields are needed to monitor local variations or to include large grains such as the Cr-doped grains. Small scanning steps were also necessary in case of small microstructures such as those studied here, in order to maintain reasonable examination times. This implies that relevant information will not be the same for all fields. The acquisition steps ranged from about 0.1 µm to 0.5 µm. An area of approximately 80 µm × 60 µm was usually covered for standard UO_2, and an area of 150 µm × 110 µm for doped large grains UO_2. Table 3 gives the zone and the radial positions for each specimen, as well as the field sizes and the scanning step sizes of the EBSD studied fields.

Table 3: EBSD map radial positions, field sizes and scanning step sizes

Label	EBSD map radial position (r/R)		Field (µm×µm)	Scanning step (µm)
Unirradiated UO_2 n°1	-		83.9×57.7	0.04
Unirradiated UO_2 n°2	-		283.8×212.5	1.35
Std-36	center	0	298.2×222.6	1.4
		0.15	56.9×42.6	0.15
Std-61	center	0	79.7×59.4	0.13
		0.14	79.4×59.8	0.10
		0.30	79.7×59.4	0.13
	intermediate	0.50	80.5×59.9	0.13
		0.58	39.8×30	0.07
	HBS transition / rim	0.75	80.1×59.7	0.13
		0.86	79.5×50.0	0.09
		1	80.2×59.7	0.13
Std-63	center	0	114×85.5	0.50
		0	56×41.3	0.35
		0.40	40.1×33.3	0.34
	rim	0.97	34.1×26.4	0.15
		1	10×10	0.07
Std-73	center	0	79.6×59.8	0.20
		0.1	107.7x57.3	0.1
		0.24	70x35	0.1
		0.3	80x60	0.1
		0.38	80×60.2	0.20
	intermediate	0.42	79.6×59.8	0.20
	HBS transition / rim	0.75	99.3x62	0.1
		1	119.7x60	0.1
Cr-35	center	0	148.8×111.8	0.86
		0.30	149×111.8	0.15
Cr-63	center	0	149.6×112.2	0.20
		0.05	132×99	0.50
		0.10	123×99	0.50
		0.15	123×99	0.50
		0.20	123×99	0.50
		0.25	123×99	0.50
		0.30	149.6×112.2	0.20
	intermediate	0.50	155.2×116.2	0.20
	HBS transition / rim	0.70	150×113.2	0.20
		1	149.8×110	0.20

4 CHARACTERIZATION TOOLS FOR THE INTERPRETATION OF EBSD DATA

EBSD data p was processed using the Channel 5 software (Oxford Instruments, Abington-on-Thames, UK) and the MTEX open source Matlab toolbox (http://mtex-toolbox.github.io/)[31]. The results obtained from the EBSD measurements and used for this study are given in this section. The goals are to:

- Detect sub-grains (with orientations close to that of the parent grain) and/or new grains (with random orientations)
- Measure the misorientations inside the initial grains
- Measure the lines of misorientation, i.e. the discontinuous misorientation, forming a network inside the initial grains.

A. Sub-grains and new grains

Grain segmentation in the EBSD maps was ensured with a misorientation threshold from sub-grain boundary to grain boundary fixed at 10°. The probability of misorientation between neighboring grains in a crystalized material with fluorite type of UO_2 was calculated with a mathematical model (Mackenzie et al.[32]). In UO_2 where the grains are randomly oriented, about 2.4% of the boundaries are expected to correspond to an angle of less than 15°, and 1% to less than 10°(Humphreys et al.[33]). The threshold for

defining grain boundaries is generally fixed at 10° or 15°. We chose the threshold of 10° to limit the grouping of two grains separated by a low-angle grain boundary. The angles above this threshold are considered as high-angle grain boundaries (HAGB) and below as low-angle grain boundaries (LAGB).
In these maps, the sub-grains are pixel clusters, inside a grain size close to that of fresh fuel and separated by closed boundaries with misorientation angles between 1 and 10°.

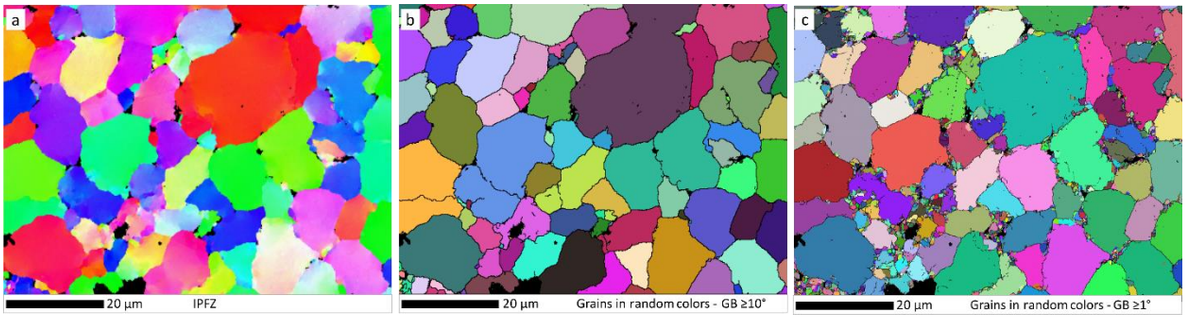

Fig.4. Std-61 - 0R, EBSD maps: (a) IPFZ with the color convention of Fig.3, (b) grains in random color with a GB misorientation threshold at 10°, (c) grains in random color with a GB misorientation threshold at 1°. The boundary misorientations above 10° are in black.

The EBSD maps (Fig.4a) are then split into grains closed by misorientation limits >10° such as initial grains of as manufactured UO_2 and new restructured grains of high burn-up fuels (Fig.4b), such as HBS grains. They are also split into grains and sub-grains closed by a misorientation limit > 1° (Fig.4c). The minimum size of a cluster (grains or sub-grains) was defined at 4 pixels. Owing to the initial size microstructure, a limit was applied considering that grains with an equivalent circle diameter (*ECD*) below 3 µm were sub-grains or new grains.
Fig.5a presents an EBSD map of Std-73 at 1R. In Fig.5b, sub-grains with a boundary misorientation of 1° and with *ECD* below 3 µm are in red, grains with a boundary misorientation of 10° and with *ECD* below 3 µm are in yellow and what remains of the parent grains are in blue. The boundary misorientations above 1° are in black as are the unindexed pores.

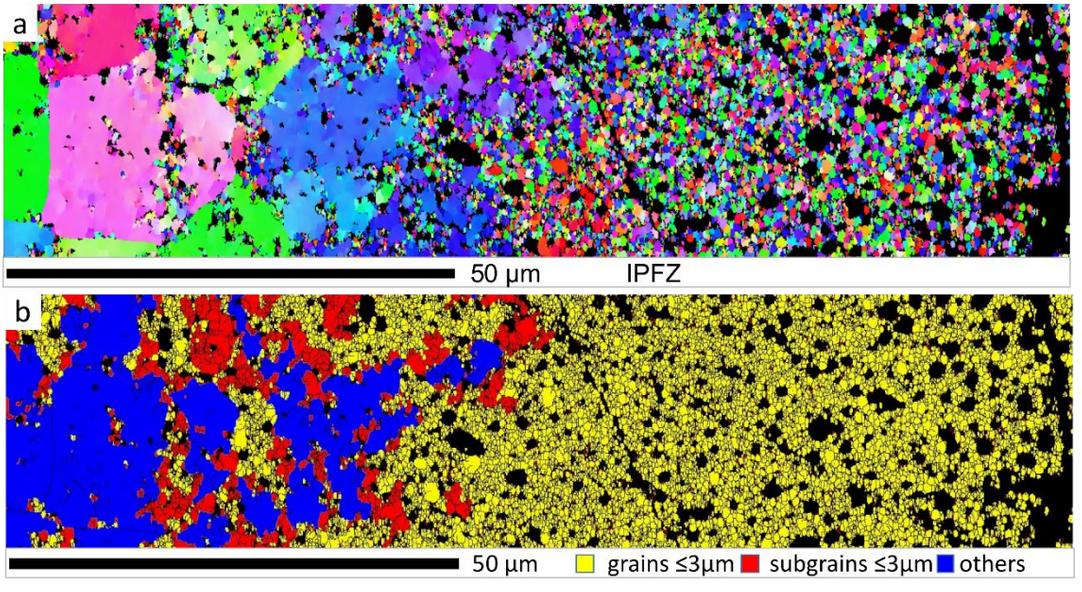

Fig.5. Std-73 - 1R. EBSD maps: (a) IPFZ, (b) restructured fractions: sub-grains with a boundary misorientation of 1° and with ECD ≤ 3 µm in red, grains with a boundary misorientation of 10° and with ECD ≤ 3 µm in yellow and the remnants of parent grains (others) in blue, the boundary misorientations above 1° are in black and the unindexed pores are also in black.

Different parameters were studied:

- The "restructured fraction 1°", calculated as the surface fraction of sub-grains, with *ECD* < 3 µm and a threshold grain boundary angle criterion at 1°
- The "restructured fraction 10°", calculated as the surface fraction of grains with *ECD* < 3 µm and a threshold grain boundary angle criterion at 10°
- In the central area, the size of the sub-grains (with ECD < 3 µm and a threshold of 1°), noted as $ECD_{50\%}$. It is the *ECD* such that 50% of the surface is covered by smaller sub-grains and 50% by larger sub-grains
- In the rim zone, the size of new grains, noted as $ECD_{50\%}$.

B. Mean and local misorientation

The average misorientation *AMis2Mean* is defined as the mean value in an EBSD map of the *Mis2Mean* measurement of each pixel: first, the grains are determined in the EBSD map and then the mean orientation of the grain is calculated. Then, the minimum rotation angle, between the pixel orientation and the mean orientation of the grain is calculated for each pixel in each grain. This difference is the *Mis2Mean*. A map of the *Mis2Mean* values (Fig.6a) is used to illustrate intragranular misorientations. The frequency of *Mis2Mean* is classified by angle class. An example of the frequency as a function of the angle class of the *Mis2Mean* determined on Std-73 at 0R map is given in Fig.6b.

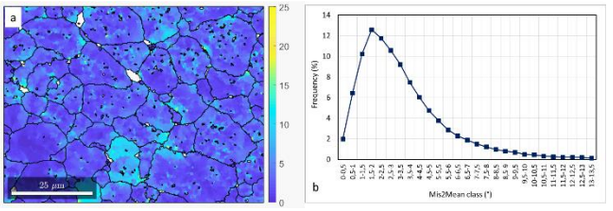

Fig.6. Std-73 - 0R. (a) Mis2Mean map, (b) Mis2Mean curve.

In *Mis2Mean* maps, double grains separated by a LAGB are removed. Such grains are pointed out by the arrows in Fig.7 with the double grains in yellow or green in the GOS (Grain Orientation Spread) map.

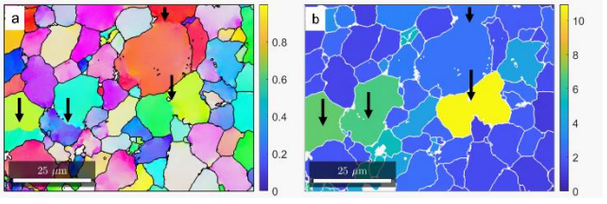

Fig.7. Std-61 - 0R. (a) IPZ map, (b) GOS map, The grain boundaries above 10° and the pores are in white. The black arrows show LAGB below 10°.

The local misorientation can also be characterized by measuring the uncorrelated misorientations between randomly chosen points in selected grains (Fig.8).

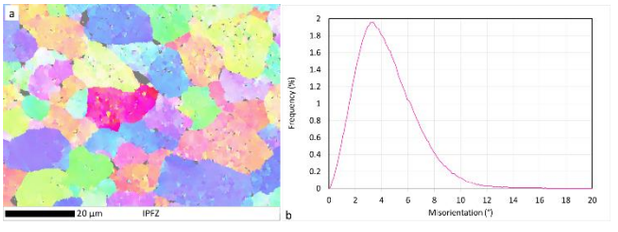

Fig.8. Std-73 – 0R. (a) selected grain in pink is highlighted, (b) uncorrelated misorientations in the selected grain.

C. Lines of misorientation

Only grains and sub-grains enclosed with continuous boundaries of more than 1° and 10° were considered for the restructured fractions. Yet in these examinations, part of the lines with a misorientation threshold

of 1° and 10° did not form closed areas. The lines of misorientations were calculated for misorientation angles of 1° (Fig.9a) and 10° (Fig.9b). Line lengths were given by the map of misorientations above 10° for HAGB (>10°) and by the difference in line lengths measured in the map of misorientations above 1° and in the map of misorientations above 10° for LAGB (1°-10°). To compare the measurements, the misorientation line lengths were normalized to the map field area. These line lengths were only measured on EBSD maps with a maximum pixel size of 0.2 µm.

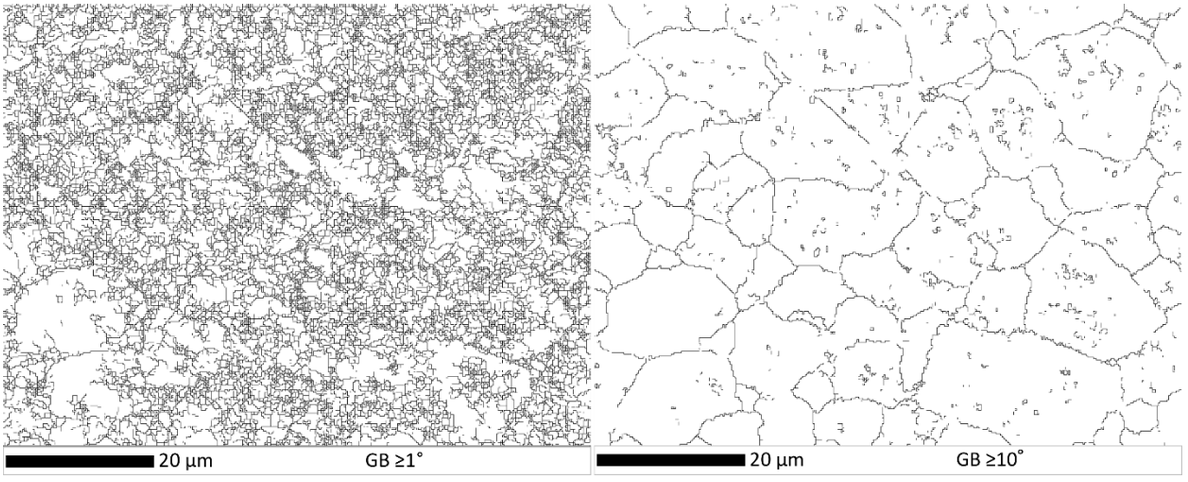

Fig.9. Std-73 – 0R. Lines of misorientation for different misorientation angles: (a) 1°, (b) 10°.

5 RESULTS

Table 4 shows the restructured fractions, the sub-grains and restructured grain sizes, the *AMis2Mean* measurements and the misorientation line lengths normalized to the field surface without the pores for standard UO_2 samples, while Table 5 shows data for Cr-doped UO_2 samples. The size of the sub-grains was measured in the central area and in the HBS transition zone while the size of the new grains was measured in the HBS transition and the rim zones, when the restructured fractions were higher than 30%.

Table 4. Restructured fractions calculated as the surface fraction of sub-grains, with ECD < 3 µm and a grain boundary threshold misorientation at 1° and 10°, sub-grain or new grain sizes in restructured zones, the average AMis2Mean of Mis2Mean curves and misorientation line lengths normalized with the field without the pores (µm/µm²) of UO_2 samples for different radial positions.

Label	Radial positions (r/R)	Restructured fraction at 1° (%)	Restructured fraction at 10° (%)	Sub-grains	New grains	*AMis2Mean* (°)	*Line misorientations (µm/µm²)*	
				$ECD_{50\%}$ (µm)	$ECD_{50\%}$ (µm)		≥10°	1°-10°
Std-0	-	0.2	0.1	-	-	0.1	0.1	0.01
Std-36	0.15	1.5	1.1	-	-	0.9	0.1	0.20
Std-61	0	13.2	3	-	-	2.2	0.3	1.3
	0.14	12.8	3.3	-	-	2.3	0.3	1.3
	0.3	20.2	4.4	-	-	2.3	0.3	1.7
	0.5	11.1	5.2	-	-	1.4	0.3	0.9
	0.58	9.7	3.5	-	-	1.5	0.4	0.9
	0.75	22.8	6	-	-	2.1	0.6	1.6
	0.86	13	6.7	-	-	1.8	0.5	1.2
	0.9825	93.1	62.1	0.6	0.6	3.5	2.9	2.1
	0.9875	98.5	83.3	-	0.6	2.7	3.6	1.7
	0.9925	100	98.4	-	0.6	1.6	4.2	1.1
	0.9975	100	100	-	0.7	1.1	4.2	0.9
Std-63	0	23.1	2.8	-	-	2.3	-	-
	1	100	100	-	0.5	1.9	4.3	2.4
Std-73	0	64.5	1.1	1.3	-	3.4	0.4	3.3
	0.1	18.3	3.5	-	-	2.6	0.3	1.4
	0.24	33.4	8.2	1.3	-	2.9	0.3	1.9
	0.3	80.9	26.5	1.2	-	6.1	0.7	3.0
	0.38	94.3	9.1	1.1	-	6.1	0.7	4.1
	0.42	10.3	2.9	-	-	1.5	0.3	0.7
	0.75	11	6.8	-	-	1.6	0.4	0.9
	0.9725	40.4	19.8	-	-	3.0	0.9	1.5
	0.9775	72.9	35.1	0.6	0.6	3.0	1.5	2.1
	0.9825	79.1	40.3	0.6	0.6	2.8	1.7	2.4
	0.9875	100	94.4	-	0.6	1.5	3.4	2.5
	0.9925	100	100	-	0.6	1.0	4.7	1.4
	0.9975	100	100	-	0.7	0.9	4.5	1.0

Table 5. Restructured fractions calculated as the surface fraction of sub-grains, with ECD < 3 µm and a grain boundary threshold at 1° and 10°, sub-grain or new grain sizes in restructured zones and the average AMis2Mean of Mis2Mean curves and misorientation line lengths normalized with the field without the pores (µm/µm²) with a misorientation above 10° or between 1 and 10° of Cr-doped UO_2 samples for different radial positions.

Label	Radial positions (r/R)	Restructured fraction at 1° (%)	Restructured fraction at 10° (%)	Sub-grains	New grains	*AMis2Mean* (°)	*Line misorientations (µm/µm²)*	
				$ECD_{50\%}$ (µm)	$ECD_{50\%}$ (µm)		≥10°	1°-10°
Cr-35	0.3	0.01	-	-	-	0.1	0.02	0.004
Cr-63	0	90.6	1.6	1.1	-	4.2	0.30	2.9
	0.05/0.1/0.15/ 0.2/0.25	-	-	-	-	4.2/4.0/3.8/2.9 /1.9	-	-
	0.3	2	0.1	-	-	0.6	0.04	0.3
	0.5	0.4	0.1	-	-	0.3	0.03	0.03
	0.7	5	0.4	-	-	0.6	-	-
	0.9675	37.9	7	0.6	-	2.4	0.5	1.6
	0.9725	58.4	14.3	0.6	-	3.1	1.5	1.1
	0.9775	72.4	23.9	0.6	-	3.6	1.1	1.9
	0.9825	81.1	39.2	-	0.6	3.4	1.5	1.7
	0.9875	98.7	80.1	-	0.7	2.7	2.6	1.3
	0.9925	100	96.2	-	0.6	1.9	3.1	0.9
	0.9975	100	100	-	0.5	1.1	3.5	0.5

D. Std samples

This part focuses on the radial changes in high burn-up Std samples.

IPFZ maps of the Std-73 sample (see Fig.10) show the radial microstructural changes in the sample, at the highest burn-up studied and partially presented in Noirot et al.[18]. The grain colors in the center of the fuel (r/R<0.4) still show initial grains of the parent fresh fuel orientation but color variations indicate misorientations and sub-grain presence in the initial grains. The relatively uniform color of the different grains shows that the microstructural changes are smaller than in the central area, in the intermediate zone at 0.42R. Restructuring can be observed, in the HBS transition and rim zones. The initial granular microstructure appears to have totally disappeared in the rim zone. The grains are restructured into small new grains with a large panel of colors. Only part of the initial grains seem to have restructured, in the HBS transition zone. Sub-grains with orientations close to their parent grains are also observed.

Based on these maps (Fig.10), Fig.11 plots Mis2Mean and uncorrelated misorientation curves, as well as *AMis2Mean*, misorientation lines and restructured fractions of the Std-73 sample for different radial positions.

Fig.11 shows a large difference between the central area and the intermediate zone. It also shows radial changes in the central area.

In Fig.11c and d, all the indicators following the degree of restructuring such as the AMis2Mean, misorientation line lengths and the restructured fractions exhibit a major drop at around 0.4R. Fig.11a shows that the increase in the AMis2Mean misorientation is due to the spreading and the shift in the maximum of the Mis2Mean curves in the central area, compared with the intermediate zone.

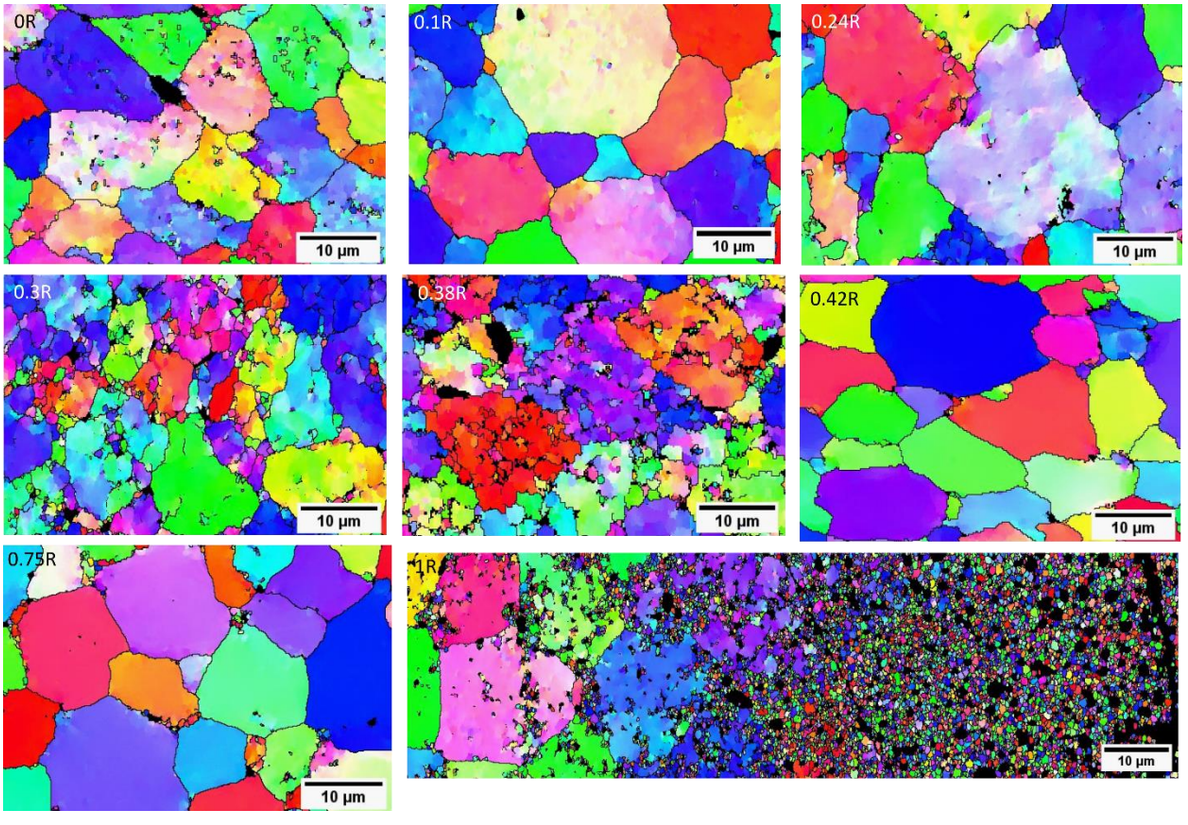

Fig.10: Std-73-0R, 0.1R, 0.24R, 0.3R, 0.38R, 0.42R, 0.75R et 1R. IPFZ maps, misorientation boundaries above 10° and the pores are in black.

Maximum restructuring in the central area is found at 0.38R on the periphery of this area. However, minimum restructuring is not at 0R but at 0.1R, which is still higher than in the intermediate zone. Uncorrelated curves of selected grains with a boundary following the parent grain boundary (see Fig.11b) show dispersion in the misorientation curves for different selected grains in the same zone. However, variations in the central area, established using the whole fields are not due to this dispersion.

A continuous increase in the restructured fractions at 10° and 1° was measured from outside the central area towards the periphery of the pellet. There is a steeper increase on the periphery. It reaches 100% at around 0.995R for the limit at 10° and at about 0.99R for the limit at 1°. The highly restructured values spread further from the periphery for the 1° limit. This will be further explained in the section on the HBS transition and rim zones.

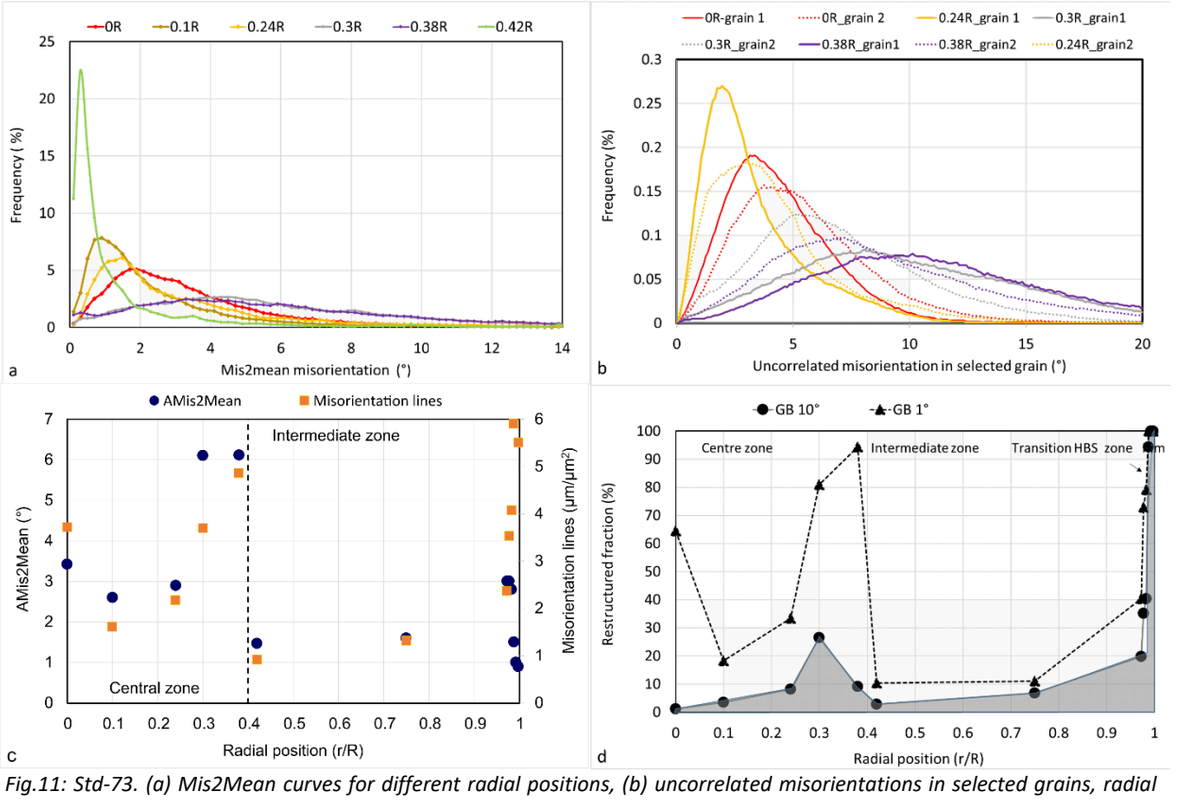

Fig.11: Std-73. (a) Mis2Mean curves for different radial positions, (b) uncorrelated misorientations in selected grains, radial profiles of the (c) AMis2Mean and misorientation lines, (d) restructured fraction for a GB of 10° and a GB of 1°.

Fig.12 displays the maps of the Std-61 sample in the central area at 0R and 0.3R and the variation in the AMis2Mean, misorientation line lengths and restructured fractions for different radial positions.

The Std-61 and Std-73 samples show similar radial changes in restructuring. As for, the Std-73 sample, measurements of the three indicators (average Mis2Mean, misorientation lines and restructured fraction) show a decrease between the central area and the intermediate zone. Restructuring in the central area is also higher at 0.3R than at 0R, as illustrated in the maps and no minimum was found between 0R and 0.3R. However, the amplitude in the change is lower in the Std-61 sample. Variations in the HBS transition zone is not monotonous towards the periphery of the pellet: there is an increase from 0.58R to 0.75R followed by a decrease from 0.75R to 0.86R, and then another increase to reach at 0.0995R, involving total restructuring into new grains.

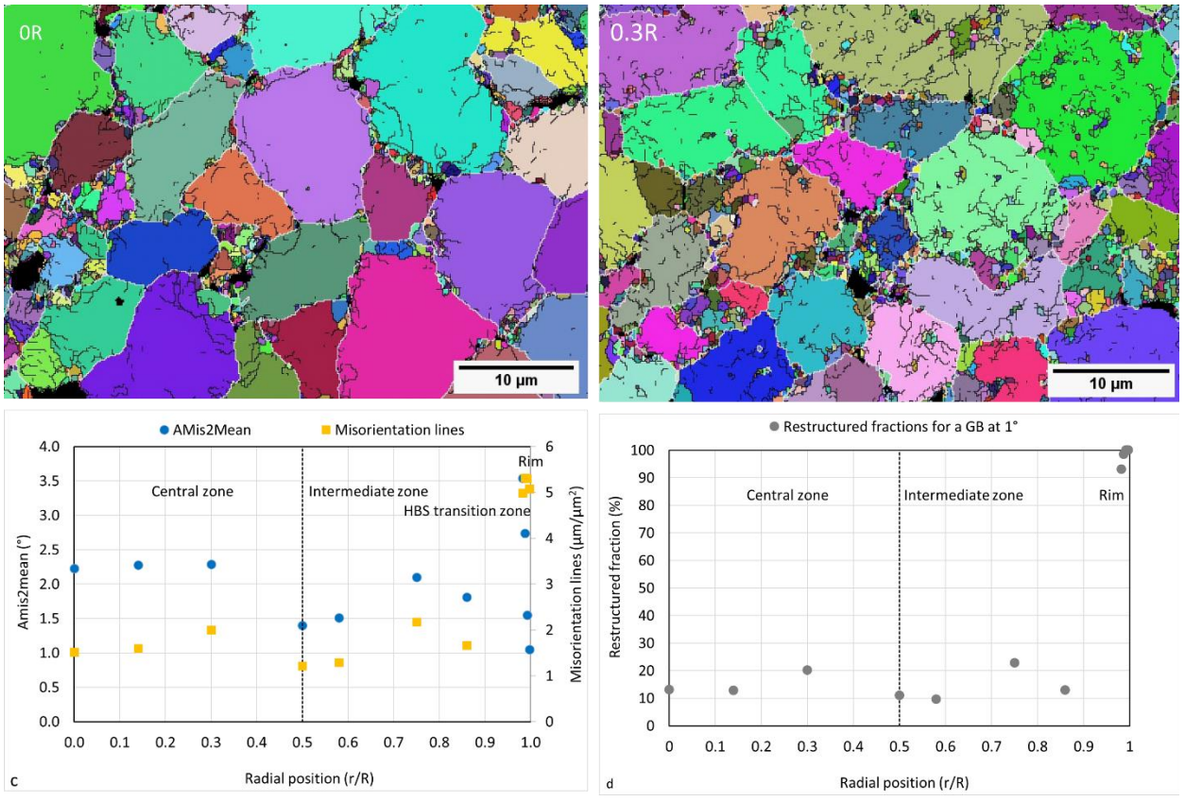

Fig.12: Std-61. (a-b) maps in random color with GB of 1° respectively at 0R and 0.3R. The misorientation boundaries above 10° are in white. The misorientation boundaries between 1°and 10 ° are in black. (c) radial profile of AMis2Mean and misorientation lines and (d) radial profile of the restructured fraction for a GB of 1°.

5.1.1 Focus on the central area

This part focuses on the central area of the fuels.

Two parent grains (see Fig.13c and Fig.13d) were extracted to analyze their misorientations locally. In the Std-73 map at 0R (see Fig.13a), the initial grains are still well delimited, using a 10° grain boundary threshold. The grain in Fig.13c at 0R was selected with a 10° grain boundary threshold. In the Std-73 map at 0.38R (see Fig.13b), some misorientation boundaries exist inside the parent grains at 10°. In Fig.13d at 0.38R, some sub-grains within the bounded grain and with a grain boundary above 10° had to be manually added to complete the initial grain to obtain the parent grain.

The misorientations of these parent selected grains in Fig.13c and Fig.13d are shown in the pole figures in Fig.13f at 0R and Fig.13g at 0.38R. Each selected grain shows a significant misorientation: the dense population of dots, corresponds to the low-angles in the curves in Fig.11a or Fig.11b, though a few dots are found a little further from the dense cloud, corresponding to the highest angles of the curves in Fig.11a and Fig.11b. Moreover, the sub-grain orientations are not dispersed over the whole pole figure even in the grain at 0.38R, where orientation spreading is maximal. This proves that no new orientation is formed independently from the parent grain. The misorientation spreads more at 0.38R than at 0R, exceeding the 10° limit that we had set. Nevertheless, all orientations exhibit a deviation around the parent orientation of the grain.

The dots, visible in Fig.13h represent the orientations of the pixels of a few selected sub-grains, as shown in Fig.13e: the misorientations are quite low in each sub-grain. Each sub-grain, as a whole, deviates from its parent grain in almost the same way. The spread of misorientation is due to the progressive tilt of sub-grains.

No specific tilt direction was found: indeed, it was checked that the sub-grains took no particular direction relative to their parent grain or to the sample orientations. They randomly spread around the parent orientation.

The size of the sub-grains was measured at different positions, in the central area. The $ECD_{50\%}$ of the sub-grains is quite constant, i.e. between 1.1 µm and 1.3 µm. Intragranular bubbles were observed on the sub-grain boundaries. Details on the bubble shapes and their variations are given in a separate paper[24].

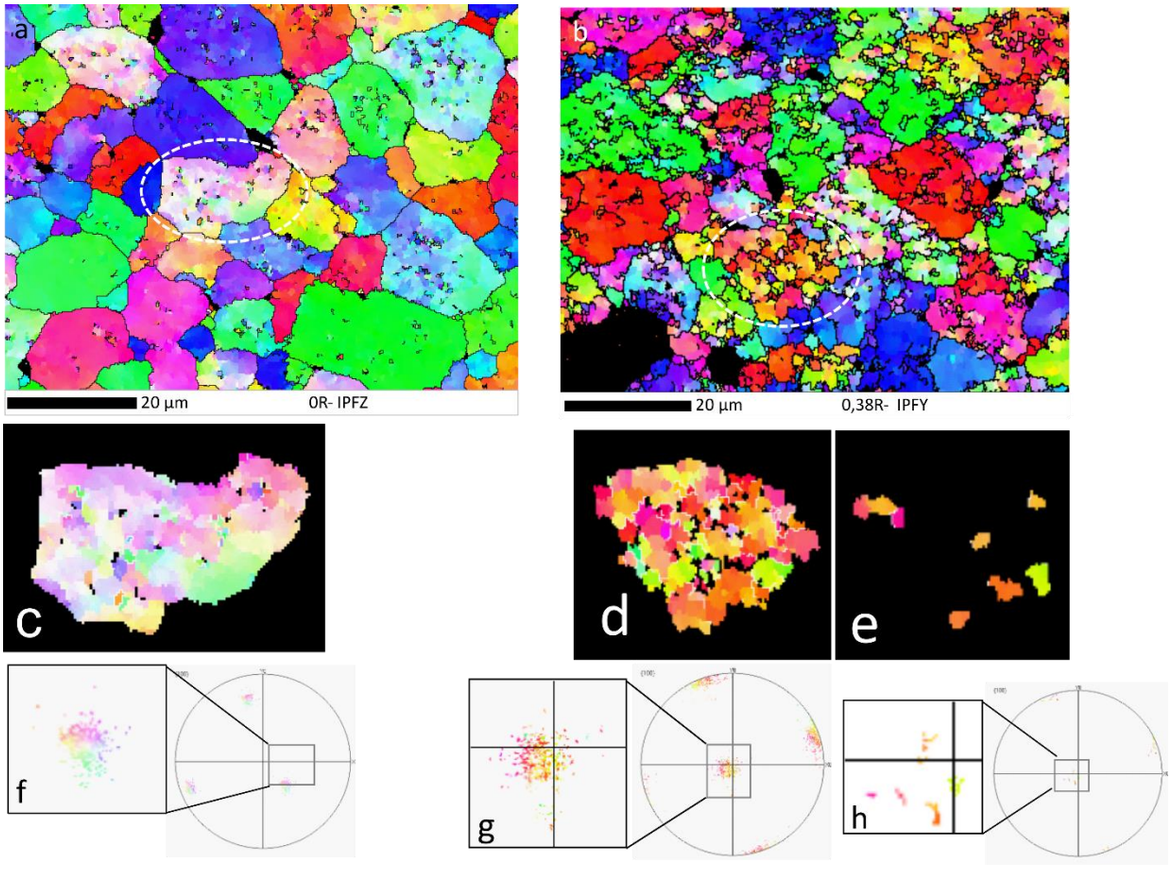

Fig.13. (a) Std-73 - 0R. IPFZ map, (b) Std-73 – 0.38R. IPFY map. The grain boundaries are in black. (c) selected grain from Fig.13a, (d) selected grain from Fig.13b, (e) selected sub-grains from Fig.13b, (f) pole figure and zoom of Fig.13c, (g) pole figure and zoom of Fig.13d, (h) pole figure and zoom of Fig.13e.

Variations in the fuel microstructure with the burn-up were studied at 0R. The *AMis2Mean* and the restructured fraction at a grain boundary of 1° increase with the burn-up (Fig.14e). At a burn-up of 36 GWd/t_U, the restructuring indicators remain low and actually increase with the high burn-up samples. The Mis2mean curves of the different high burn-up samples in Fig.14d show that deviation from the initial orientation also progressively increases at 0R: with the burn-up, the Mis2Mean curves spread further and the maximum shifts to higher angle misorientation.

The restructuring maps of high burn-up Std samples in Fig.14 show that restructuring starts on the grain boundaries or near pores. Restructuring spreads to the grain boundaries (Fig.14a) and to the interior of the grains with the increase of the burn-up (Fig.14b and Fig.14c).

The measured restructured fraction of Std-61 is low and mainly along the grain boundaries at 0R. Nevertheless, the *Amis2mean* indicator shows significant misorientation. 3D FIB-SEM examinations also showed a high density of lenticular bubbles inside these grains. The misorientation and the bubble shapes point to restructuring with boundaries at angles below 1° (not detectable with the sensibility of this EBSD device applied to irradiated fuel).

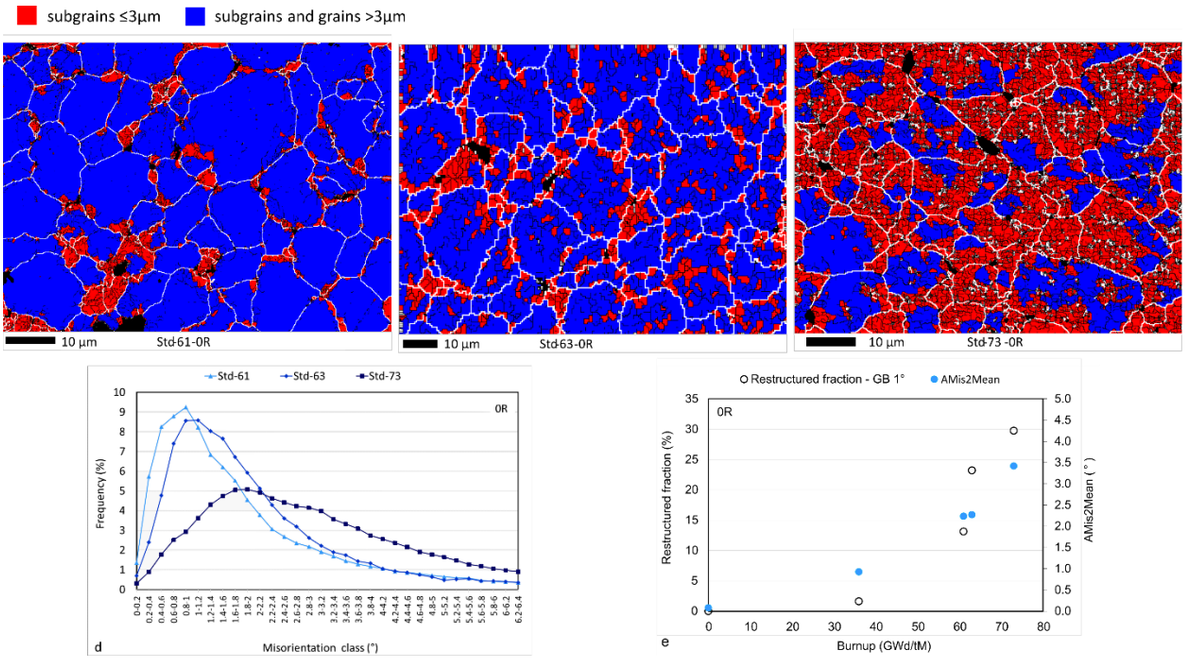

Fig.14. 0R. (a, b, c) Std-61, Std-63 and Std-73, restructured fraction at GB>1° maps: sub-grains with a closed grain boundary misorientation > 1° and with ECD < 3 µm in red, and the remnants of parent grains in blue, misorientation boundaries above 10° in white, misorientation boundaries between 1° and 10° in black and unindexed pores in black. (d) Std-61, Std-63 and Std-73, Mis2Mean curves (e) variation in the AMis2Mean and the restructured fraction of Std samples with the burn-up.

5.1.2 Focus on the intermediate zone

Different maps of Std samples in the intermediate zone are presented in Fig.15. The grain boundaries are quite straight in fresh fuel (Std-0), whereas the grain boundaries are rounded and undulated in irradiated fuels. This is observed both in the intermediate zone and in the central area. This curvature was also observed in the Std-36 sample (Fig.15). This points to the existence of small grain boundary displacements during irradiation.

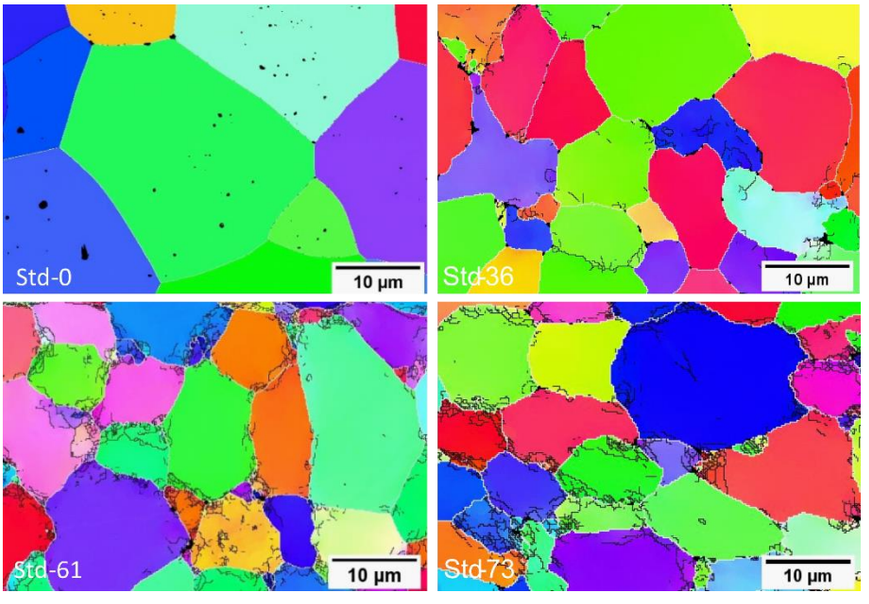

Fig.15. Std-0, Std-36-0.15R, Std-61-0.5R, Std-73-0.42R. The misorientation boundaries above 10° are in white. The misorientation boundaries between 1°and 10 ° are in black.

Microstructural changes occurring with the burn-up in the intermediate zone, are small, as indicated by the *Amis2mean* and the misorientation lines in Fig.16a and Fig.16b. They differ greatly from variations in the central area, as already seen by Gerczak et al.[17] at 0.63R and Cappia et al.[19] at 0.6R. Moreover, Fig.16c compares the uncorrelated curves of the misorientations in a whole grain surface and in a surface restricted to the center of the same grain. The center of the grain exhibits less misorientation than its periphery.

The small misorientations, that we measured in our work, are mainly located near the grain boundaries. This is in agreement with misorientation lines above 1°, observed near the grain boundaries of all irradiated Std samples in Fig.15. The right side of the EBSD KAM map (Kernel Average Misorientation = average of the misorientation between the center and all the neighbors in a defined grid of several pixels) at 0.55R-0.6R in Cappia et al.[19] also showed that the grains were not internally sub-divided and that the local distortion was mainly confined along the original grain boundary. In Gerczak et al.[17] study, however, restructuring did not seem to be preferentially located near the grain boundary.

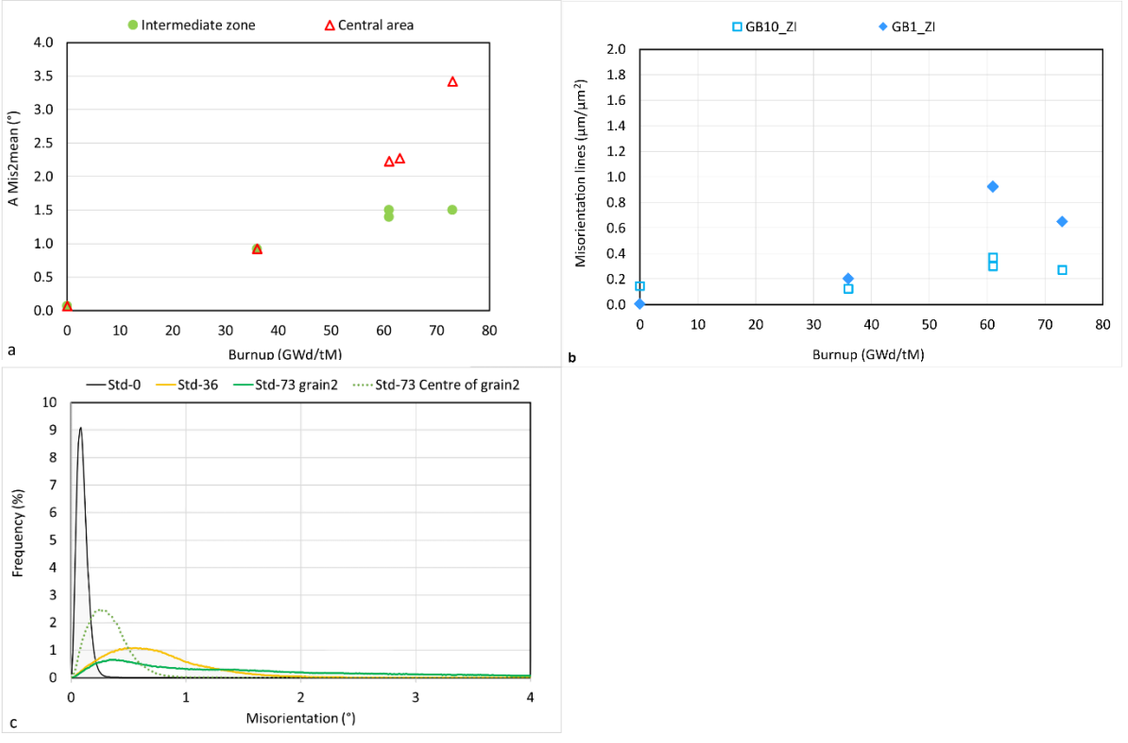

Fig.16. (a) Comparison of variations in the Amis2mean of Std samples with the burn-up in the center (0R) and in the intermediate zone, (b) misorientation lines with GB of 10° or 1° as a function of the burn-up in the intermediate zone, (c) comparison of uncorrelated misorientations of selected grains in a whole grain, in the center of the same grain of Std-73 and in a grain of Std-0 and Std-36. The high burn-up samples of the intermediate zone are defined in Table 3.

5.1.3 Focus on the HBS transition and rim zone

The transition between the intermediate zone and the HBS transition zone is progressive. In the first step of restructuring at 0.75R (see Fig.17 for Std-61 sample and for Std-73 sample), restructuring (in red for the sub-grains and yellow for the new grains) seems, as in the central area, to start along the grain boundaries and near large pre-existing pores and to extend inside the grains. Nevertheless, significant sections of the grain boundaries did not undergo restructuring.

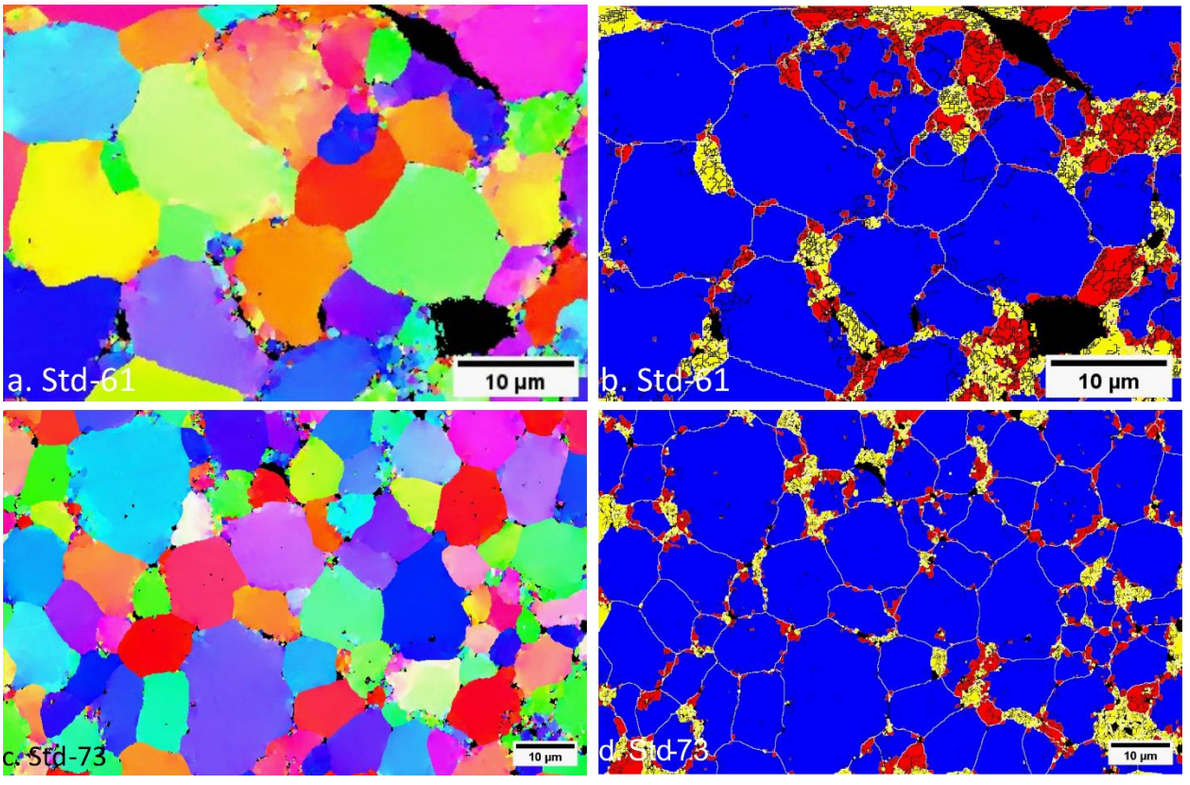

Fig.17. Std-61–0.75R and Std-73–0.75R. (a, c) IPFZ maps, (b, d) Restructuring fractions: sub-grains with a misorientation boundary > 1° and with ECD < 3 µm in red, grains with a misorientation boundary of 10° and with ECD < 3 µm in yellow and the remnants of parent grains in blue, misorientation boundaries above 10° are in in white, misorientation boundaries between 1° and 10° and unindexed pores are in black in black.

Fig.18 and Fig.5 show EBSD maps of the HBS transition and rim zones in Std-61 and Std-73 respectively. Variations in the HBS formation are progressive (Fig.5 and Fig.18b). On the left side of the map in Fig.18b, parent grains can be seen to have partially restructured into sub-grains with LAGB shown in red. The remnant unrestructured parts of parent grains are shown in blue. Sub-grains progressively disappear towards the periphery to form HBS with sub micrometric grains with HAGB (in yellow). The initial granular microstructure has totally disappeared in the rim zone (right side of the maps).

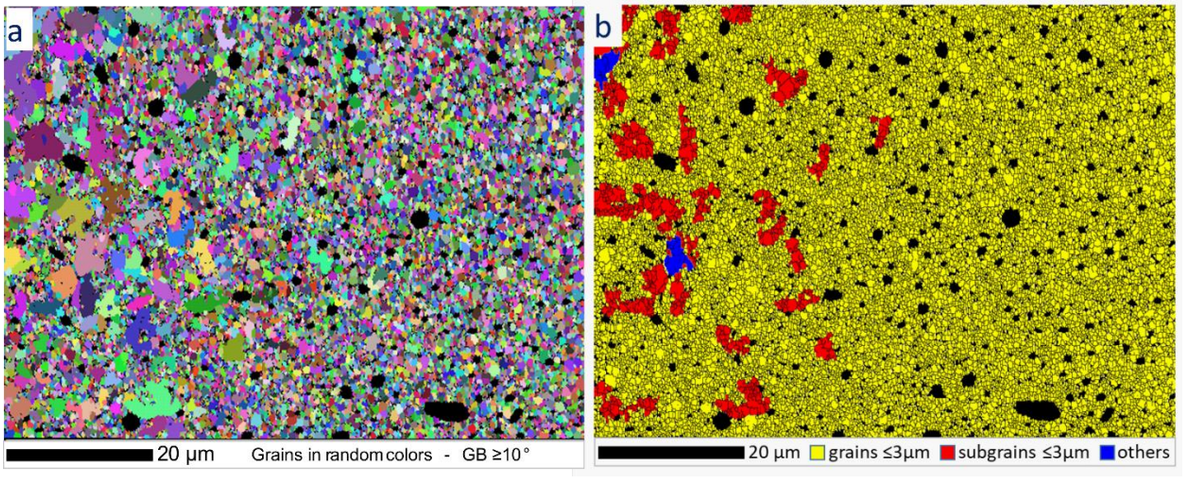

Fig.18. Std-61 - 1R, EBSD maps: a. grains in random color with a GB threshold at 10°, b Restructured fractions: sub-grains with a grain boundary misorientation > 1° and with ECD ≤ 3 µm in red, grains with a grain boundary misorientation of 10° and with ECD ≤ 3 µm in yellow and the remnants of parent grains (others) in blue, the misorientation boundaries ≥ 1° are in black and the unindexed pores is also in black.

Fig.19 shows different uncorrelated misorientation curves for the rim and other areas selected, to correspond as much as possible to parent grains (zones 2 to 5) or remnants of parent grains (zone 1). The zones 2 through 5 were drawn manually because the high level of restructuring prevents extracting the boundary of the whole parent grains: many small areas with close orientations were considered as belonging to the same parent to determine different zones. With respect to the rim, the uncorrelated curve of misorientations is in good agreement with the theoretical distribution of grain boundary misorientations, between two neighboring grains, in a randomly oriented grain material, and for a cubic crystal structure[32]. The new grains follow a random statistical orientation and they tend to have lost their link with the parent grain's initial crystal orientation.

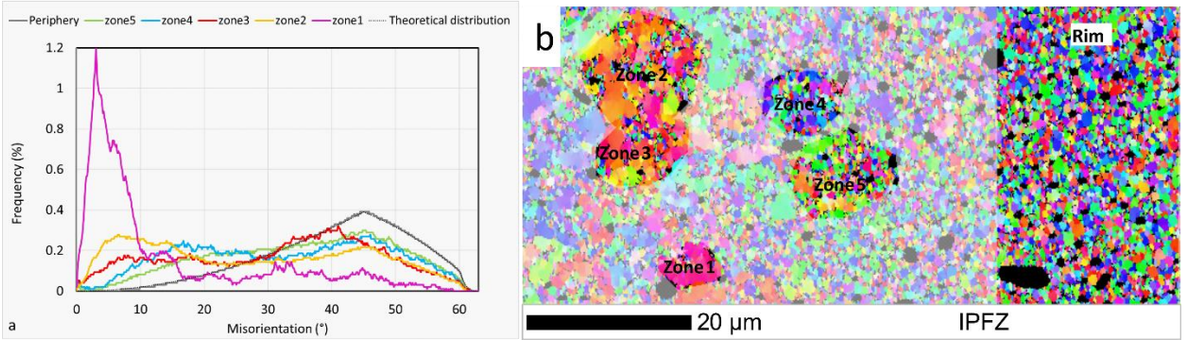

Fig.19. 1R - Std-61. (a) Uncorrelated misorientations of different selected zones and theoretical distribution of grain boundary misorientations, between two neighboring grains in a randomly oriented grain material, for a cubic crystal structure[32], (b) selected zones in the IPFZ map.

In the HBS transition zone, the curves of zones 2 to 5 show a misorientation at a low-angle of sub-grains in the initial grains. In fact, each curve of uncorrelated misorientation is a sum of two components: one similar to the randomly oriented grains found on the extreme periphery, the other similar to that obtained in the central area with dispersion around the parent grain orientation. The general trend is that the further the field is from the periphery, the lower the first random component and the higher the second dispersion. Misorientation is already high in zone 1, which corresponds to the remaining part of an initial grain, without identified sub-grains.

Fig.20 shows the radial restructuring changes in the rim and HBS transition zones for the Std-61 and the Std-73 samples. The limit of total restructuring in random grains (RF 10°) is around 0.9925R for both Std samples. The fuel is totally restructured in the sub-grains and grains (RF 1°) at 0.9875R. The size of the

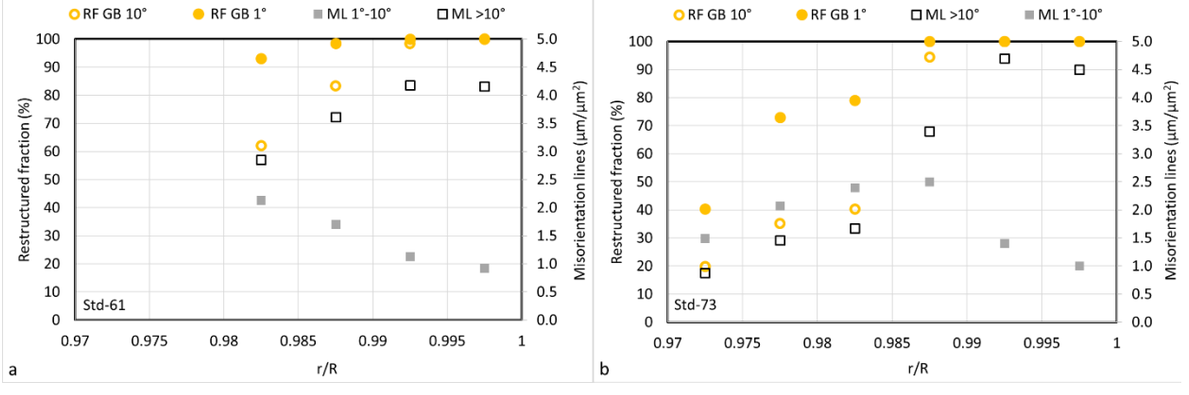

Fig.20. 1R (a) Std-61, (b) Std-73. Restructured fraction (RF) and misorientation lines (ML) for different radial positions with boundary thresholds of 10° and 1°.

new grains was measured: the $ECD_{50\%}$ at 10° is 0.6 µm for Std-61, 0.5 µm for Std-63 and 0.8 µm for Std-73. This size does not seem to evolve with the burn-up.

E. Cr-doped samples

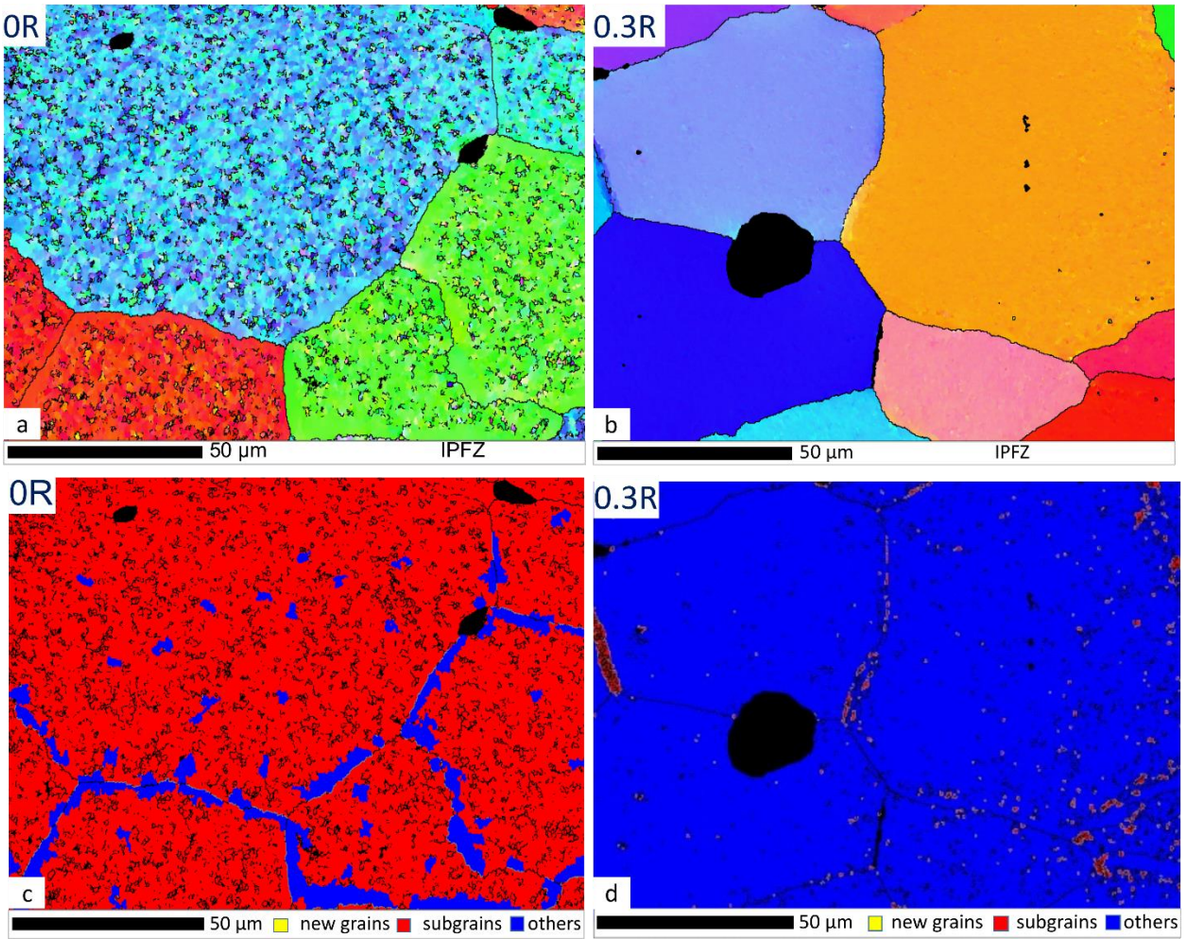

Fig.21: Cr-63. (a-b) IPFZ maps at 0R and 0.3R the misorientation boundaries ≥ 10° are in black, (c-d) Restructured fractions at 0R and 0.3R. Sub-grains with a misorientation boundary > 1° and with ECD < 3 µm in red, and the rest in blue, misorientation boundaries above 10° and unindexed pores in black.

The radial changes in the Cr-63 sample (Fig.22**)** differ from those in the Std samples. The figure shows a progressive decrease in the measurements from 0R to 0.3R and to 0.5R in the intermediate zone where the lowest level is reached.

At 0R, the grains are almost totally restructured in sub-grains with orientations, similar to that of the parent grains (Fig.21a). Only the near boundary area of the grain is not restructured (Fig.21c). There are also fewer bubbles in this area. This effect was not observed in Std samples. The $ECD_{50\%}$ of the Cr-63 sub-grains at 0R is 1.1 µm. The sizes of the sub-grains in the two types of fuel are very close, despite very different initial grain sizes. Restructuring in the Cr-63 sample at 0R is higher than that in Std samples at 0R, but similar to that in Std-73 at 0.38R.

As shown in Fig.21b and d, no restructuring is measured at 0.3R. In Fig.23, however, the uncorrelated curve for Cr-63 curve at 0.3R shows significant misorientation in the initial grain. It seems to be more sensitive than the restructured fraction because there is no cut-off at 1°. The uncorrelated misorientation curve at 0.3R spreads more than the curve at 0.5R and more than the Cr-35 curve. 3D SEM-FIB examinations[24] show a high density of lenticular bubbles inside these grains at 0.3R. Their shapes suggest

that they are likely to be on boundary surfaces with a misorientation threshold below 1°. This situation is similar to that of Std-61 at 0R.

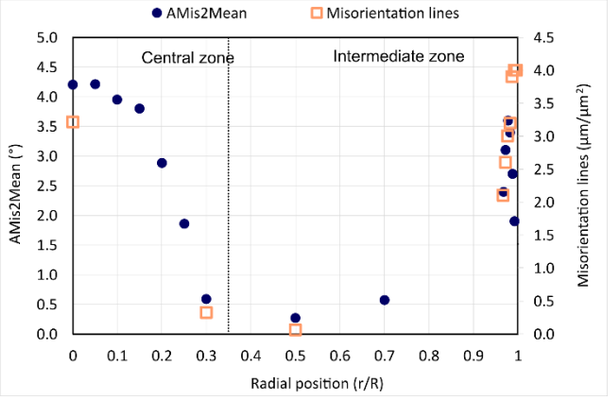

Fig.22: Cr-63. Radial profile of AMis2Mean and misorientation lines.

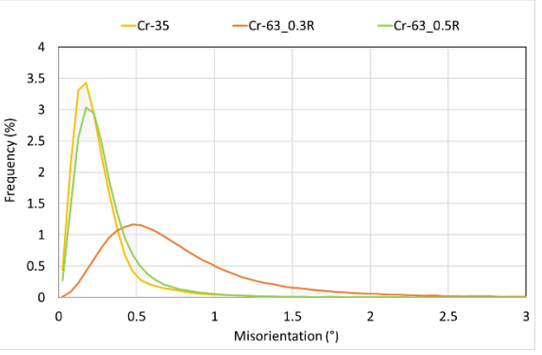

Fig.23: Cr-35 and Cr-63. Uncorrelated misorientations of selected grains.

In the intermediate zone of the Cr-63 sample, the change between Cr-63 at 0.5R (Fig.24b) and Cr-35 (Fig.24a) is low. The uncorrelated curves in Fig.23 (Cr-35 and Cr-63 at 0.5R), the *AMis2Mean* and the misorientations lines in Table 5 are all similar. No restructuring is observed, which differs from the high burn-up Std samples that showed restructuring near the grain boundary. The grain boundaries are more undulating at high burn-up than at 35 GWd/t_U.

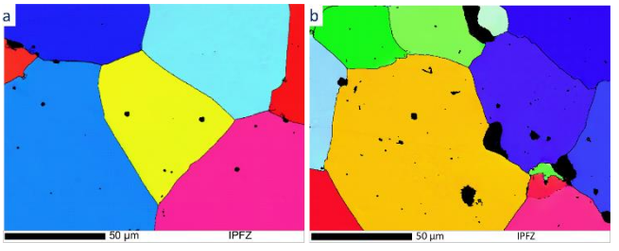

Fig.24: IPFZ maps. (a) Cr-35-0R, (b) Cr-63-0.5R. Misorientation boundaries above 1° are in black.

Fig.25 shows the periphery of Cr-63. The same detailed observations recorded for Std samples also apply to the HBS transition zone and the rim of the Cr-63 sample, i.e. emergence of sub-grains with orientations similar to that of the parent grain (red in Fig.25b), and new restructured grains with random orientations independent from those of the parent grain (yellow in Fig.25b). Significant misorientations in the remnants of the initial grains were measured without sub-grains. Nevertheless, sub-grains with boundary misorientations below 1° possibly exist. The extent of restructuring in the Cr-63 sample is similar to that found in Std samples. However, the onset of restructuring is located in a different area to that of the Std samples: it starts either along the grain boundaries or inside the grains (red in Fig.25b), leaving long sections of unrestructured grain boundary zones.

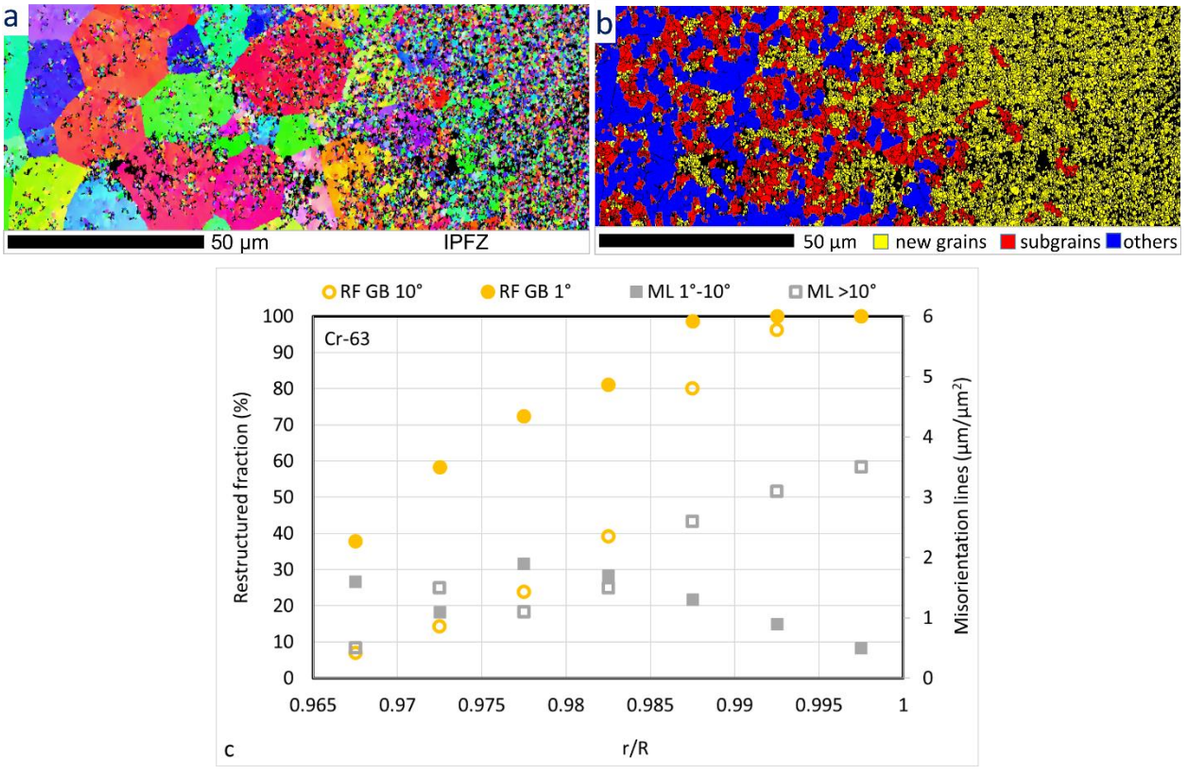

Fig.25. Cr-63 – 1R. (a) IPFZ map, (b) Restructured fractions: sub-grains with a grain boundary misorientation > 1° and with ECD < 3 µm in red, grains with a grain boundary misorientation >10° and with ECD < 3 µm in yellow and the remnants of parent grains (others) in blue, misorientation boundaries between 10° in white, misorientation boundaries between 1° and 10° in black and unindexed pores in black, (c) Restructured fraction (RF) and misorientation lines (ML) for different radial positions with boundary thresholds of 10° and 1°.

6 DISCUSSION

Four standard UO_2 fuel samples, with burn-ups of 36, 61, 63, and 73 GWd/t_U and two Cr-doped UO_2 fuel samples with burn-ups of 35 and 63 GWd/t_U were used to study radial changes in the microstructure due to irradiation using EBSD. As expected, HBS formation occured on the periphery of all samples with a burn-up above 61 GWd/t_U. Similarly, these examinations showed that a restructuring occurred in the central area of the pellets for the same samples.

The results of this work can be compared with those detailed in the Gerczak et al.[17] paper on the restructuring of a high burn-up sample, irradiated at 72 GWd/t_U using SEM/EBSD and TEM. The article mainly focused on HBS transition and rim zones. However, Gerczak et al.[17] also measured the radial profile of misorientations lines and grain / sub-grain sizes in their EBSD maps. They defined a minimum threshold boundary at 2°, whereas our minimum threshold boundary that doesn't take into account noise and highlights maximum restructuring and sub-grain formation was defined at 1°. Concerning HBS transition, Gerczak et al.[17] showed the impact of LAGBs on the degree of restructuring, comparing the EBSD grain color map with a minimum misorientation angle up to 1°.

The results of this work can also be compared with the Cappia et al. study[19] regarding the EBSD and TEM characterization of a PWR high burn-up sample, irradiated at 76 GWd/t_U . They showed the IPFZ and KAM maps of the three different zones, which we defined in this study as the central area, intermediate zone and rim zone. The minimum misorientation between grains and sub-grains were 3°in this study. Lamellas were also prepared in each zone and observed in TEM.

F. Restructuring on the periphery

Fig.26a and Fig.26b summarize the EBSD study in the HBS transition and rim zones.

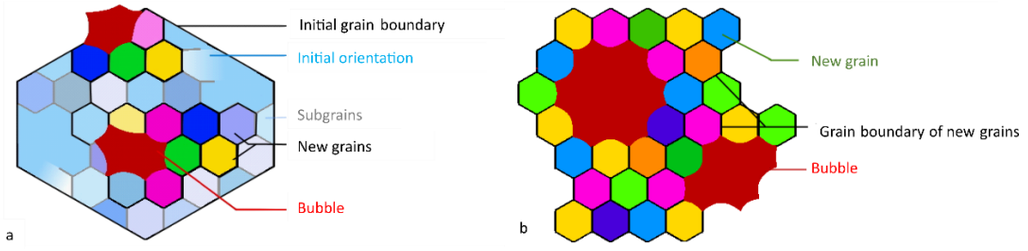

Fig.26. High burn-up restructuring in the periphery: (a) HBS transition, (b) rim.

The maximum local burn-up of the samples, reached at 1R, was measured with EPMA Nd profiles at 109 GWd/t_U for Cr-63, 115 GWd/t_U for Std-61, 121 GWd/t_U for Std-63 and 152 GWd/t_U for Std-73 respectively.

Microstructural changes on the periphery can be described as forming a series of steps[17]. It starts with a misorientation of the local crystal orientation inside the grains (possibly including sub-grains formed with LAGB below 1°). This misorientation remains similar to the orientation of the initial grains. Pockets of LAGB sub-grains, with orientations still similar to those of the initial grains, are then formed (Fig.26a) as already shown by Bengtsson et al.[15], Sonoda et al.[9], Gerczak et al.[17]. This sub-division of parent grains into sub-grains with LAGBs is probably due to a polygonization mechanism with an arrangement of dislocations at the sub-grain boundaries[14,34]. Within these pockets, sub-micrometric grains with HAGB of random orientations then form, as shown by Bengtsson et al.[15], Gerczak et al.[17] and Cappia et al.[19]. This spreads to fill the whole volume in the end (Fig.26b).

The restructured zones, both in weakly misoriented sub-grains or in the new grains of random orientations, are systematically co-located with the fission gas bubbles (Fig.26), as previously shown[9,11,17,18,35].

The onset of restructuring in these Std samples occurs along the grain boundaries and near pre-existing pores. This onset along the grain boundaries had already been demonstrated in previous papers by Une et al.[7] and Bengtsson et al.[15]. In the Gerczak et al. study[17], restructuring appeared to start at the parent grain boundaries in the HBS transition zone and mid-radial regions of the fuel specimen, as well as in the intragranular regions and there is no clear insight on the role of pre-existing pores. Noirot et al.[11] showed in another Std UO_2 sample, that the formation of HBS did not especially start at the grain boundaries. In Noirot et al.[35], HBS was partially formed in a standard UO_2 sample and in an undoped large grain UO_2 sample. Small pockets of HBS were found all over the surface of the standard UO_2 sample. A very local HBS formation occurred along all the grain boundaries in the undoped large-grain UO_2, but pockets of HBS started to form in the very central part of the grains, with no link to the grain boundaries. It therefore seems that grain boundaries and near pre-existing pores are preferential sites for HBS formation in many fuels but not seems to be true for all fuels.

With respect to the Cr-doped UO_2 sample studied in this article, the onset of restructuring occurs inside grains and near pre-existing pores. Baron et al.[12] investigate another example of a high burn-up chromium doped large grain UO_2 fuel with a partially formed HBS, mainly inside grains, and with most of the grain boundaries remaining unaffected by HBS formation. It therefore seems that Cr doping promotes intragranular HBS formation, compared with undoped fuels where grain boundaries tend to promote it.

The size of the sub-grains and new grains in the HBS transition zone and the rim tends to be similar, i.e. around 0.6 µm, whatever the initial microstructure. This size of the grains is equal to the size of the grains calculated by Gerczak et al.[17] in HBS with misorientation above 15°. It is smaller than the size of the sub-grains in the central area, as also shown by TEM in Cappia et al.[19] . This size is also relatively constant with the burn-up and the distance from the periphery. However, Noirot et al.[11] showed that sub-grain sizes in heterogeneous MOX Pu agglomerates were larger for higher irradiation temperatures found in Pu rich agglomerates further from the rim of the pellet. Cappia et al.[19] showed that there was no network of extended defects in the HBS grains. However, small loops and defects can still be seen in the grains that could be damaging due to FIB milling. TKD[17] and TEM[9] examinations showed a fine-grain grain structure between 150-350 nm, surrounding the circumference of the large pores. These fine grains surrounding the pores were not clearly defined by EBSD, probably due to its resolution limitations relative to tKD and TEM.

The extent of restructuring in the Cr-63 sample is similar to that in Std samples. This result differs from the results reported by Baron et al.[12] and showing accelerated HBS formation on the periphery of another Cr-doped UO_2.

G. Restructuring in the central area

The EBSD results allow us to describe the high burn-up microstructure in the central area, as shown in Fig.27.

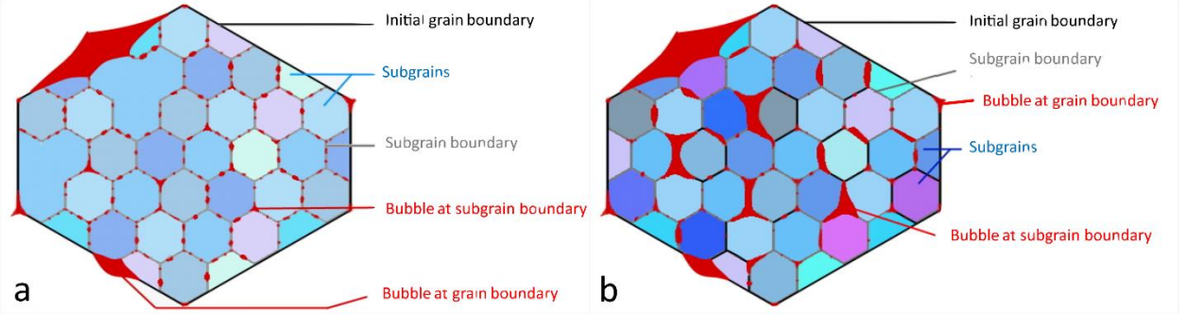

Fig.27. High burn-up restructuring in the central area: (a) 20%-60% restructuring, (b) 90% restructuring

The fuel restructures into sub-grains in the central area at high burn-up and high temperature. These sub-grains with LAGB were also observed in Gerczak et al.[17] and Cappia et al.[19] studies on the central area. Only small changes were measured in the intermediate zone, with the same burn-up but the coldest temperature. The abrupt change in the center could therefore be considered as a coupled effect of a high burn-up and high temperature.

In our work, however, the periphery of the central area (Fig.27a) in the Std samples tends to be more restructured than 0R (Fig.27b). Additionally, a minimum of around 0.1R was found for Std-73 for which radial changes were measured with more fields. This effect was not investigated in the Gerczak et al. study[17], because 0R to 0.25R was lacking in the sample in question. Maximum restructuring was found in the center of the Cr-63 sample, with a progressive decrease from 0R to 0.4R. Concerning each sample, the zone where maximum restructuring could be observed was also the zone where the bubbles were the largest. This implies that temperature and burn-up are unlikely to be the only parameters involved.
Cappia et al.[19] also observed that the LAGB was more extensive on the periphery of the central area (0.55R) than at 0.26R. Yet, there was a major difference in the microstructure of the samples in the central zone. The bubbles at 0.26R were larger than at 0.5R in Cappia et al.[19], whereas the bubbles on the periphery of the central zone were larger than at 0R in our work[24]. In Cappia et al.[19], the RGF of the rod

was 16%, suggesting that the irradiation temperature was higher than in our study where the maximum RGF of the rods was 6.2%. This shows that in addition to mechanisms involving restructuring and large bubbles formation, higher central temperatures in the fuel studied by Cappia et al.[19] promoted fission gases diffusion and bubble growth. As Cappia et al.[19] suggested, thermal recovery could have annealed the defects responsible for the sub-grain boundaries and promoted fission product diffusion to create the bubbles, in the center of the pellet where the temperature is higher.

The sub-grain size (ECD) tended to be around 1 µm, whatever the sample burn-up and the initial microstructure. In all high burn-up irradiated fuels, sub-grains tended to have orientations distributed around the parent grain that spread further with the increasing burn-up. No sub-grain growth was measured. As on the periphery, this sub-division into sub-grains with LAGBs was probably due to a polygonization mechanism with the arrangement of dislocations forming the sub-grain boundaries[14,34]. These sub-grains were detected in our study with a misorientation boundary limit of 1°. However, it is likely that sub-grains exist with misorientation boundaries below 1° and therefore not detectable with our EBSD technique used in a nuclear environment. This is particularly the case in Std-61 at 0R and Cr-63 at 0.3R where uncorrelated misorientation curves show a significant misorientation in the initial grains but only a little sub-grain formation could be evidenced, whereas the 3D FIB-SEM examinations show a high density of lenticular bubbles inside these grains[24]. Such bubbles are likely to be on sub-grain boundary surfaces. TEM examinations in the central area could provide us with the missing information. As on the periphery, the onset of restructuring seems to differ between the Std samples and Cr-doped samples. Restructuring in our Std samples started along the grain boundary or near pre-existing pores. Restructuring in the high burn-up Cr sample tended to start inside the grains and a section near the grain boundary was not restructured.

7 CONCLUSION

The EBSD technique was applied to a set of irradiated UO_2 samples, at a burn-up between 35 and 73 GWd/tU, including Std UO_2 and Cr-doped UO_2 samples. Unirradiated UO_2 samples were also used as reference. In parallel to 3D FIB-SEM examinations of the fission gas bubbles[24], our work confirmed information on the formation of HBS on the periphery of high burn-up UO_2: misorientations in the parent grains, formation of sub-grains with orientations spread around the parent grain orientations and formation of randomly oriented grains spreading over the whole rim. It showed that restructuring in the central area, associated with bubble formation, existed in all studied samples with a burn-up above 61 GWd/tU whatever their initial microstructure, and that this increased with the increasing burn-up. This restructuring sub-divided the initial grains into sub-grains with orientations similar to that of the parent grains. The detailed characterizations evidenced radial variations in the central area of the Std samples. These radial changes and differences between the samples showed that burn-up and temperature were unlikely to be the only parameters involved.

ACKNOWLEDGMENTS

The authors are thankful to EDF and FRAMATOME for their support in the studies of these irradiated fuels that they manufactured and used in commercial French nuclear power plants.

CONFLICT OF INTEREST

The authors have no conflict of interest to declare.

REFERENCES

[1] K. Nogita and K. Une, Nucl. Inst. Methods Phys. Res. B **91**, 301 (1994).
[2] K. Nogita and K. Une, J. Nucl. Mater. **226**, 302 (1995).

[3] J. Spino, K. Vennix, and M. Coquerelle, J. Nucl. Mater. **231**, 179 (1996).
[4] H. Matzke and M. Kinoshita, J. Nucl. Mater. **247**, 108 (1997).
[5] H. Matzke and J. Spino, J. Nucl. Mater. **248**, 170 (1997).
[6] K. Nogita, K. Une, M. Hirai, K. Ito, K. Ito, and Y. Shirai, J. Nucl. Mater. **248**, 196 (1997).
[7] K. Une, M. Hirai, K. Nogita, T. Hosokawa, Y. Suzawa, S. Shimizu, and Y. Etoh, J. Nucl. Mater. **278**, 54 (2000).
[8] J. Spino and D. Papaioannou, J. Nucl. Mater. **281**, 146 (2000).
[9] T. Sonoda, M. Kinoshita, I.L.F. Ray, T. Wiss, H. Thiele, D. Pellottiero, V. V. Rondinella, and H. Matzke, Nucl. Instruments Methods Phys. Res. Sect. B Beam Interact. with Mater. Atoms **191**, 622 (2002).
[10] J. Spino, A.D. Stalios, H. Santa Cruz, and D. Baron, J. Nucl. Mater. **354**, 66 (2006).
[11] J. Noirot, L. Desgranges, and J. Lamontagne, J. Nucl. Mater. **372**, 318 (2008).
[12] D. Baron, M. Kinoshita, P. Thevenin, and R. Largenton, Nucl. Eng. Technol. **41**, 199 (2009).
[13] J. Noirot, I. Aubrun, L. Desgranges, K. Hanifi, J. Lamontagne, B. Pasquet, C. Valot, and P. Blanpain, Nucl. Eng. Technol. **41**, 155 (2009).
[14] V. V. Rondinella and T. Wiss, Mater. Today **13**, 24 (2010).
[15] S. Bengtsson, in *AIEA Tech. Commitee Meet. Adv. Pellet Technol. Improv. Perform. High Burn. Tokyo* (1996), pp. 149–160.
[16] D. Jädernäs, F. Corleoni, A. Puranen, M. Granfors, G. Lysell, P. Tejland, D. D. Lutz, and L. Hallstadius, Topfuel, Charlotte, NC, (2013).
[17] T.J. Gerczak, C.M. Parish, P.D. Edmondson, C.A. Baldwin, and K.A. Terrani, J. Nucl. Mater. **509**, 245 (2018).
[18] J. Noirot, I. Zacharie-Aubrun, and T. Blay, Nucl. Eng. Technol. **50**, 259 (2018).
[19] F. Cappia, K. Wright, D. Frazer, K. Bawane, B. Kombaiah, W. Williams, S. Finkeldei, F. Teng, J. Giglio, M.N. Cinbiz, B. Hilton, J. Strumpell, R. Daum, K. Yueh, C. Jensen, and D. Wachs, J. Nucl. Mater. **569**, 153881 (2022).
[20] M. Teague, B. Gorman, B. Miller, and J. King, J. Nucl. Mater. **444**, 475 (2014).
[21] D. Frazer, F. Cappia, J.M. Harp, P.G. Medvedev, K.J. McClellan, S.L. Voit, J. Giglio, D. Jädernäs, and P. Hosemann, J. Nucl. Mater. **562**, 153545 (2022).
[22] J. Noirot, L. Noirot, L. Desgranges, J. Lamontagne, T. Blay, B. Pasquet, and E. Muller, in *Proc. 2004 Int. Meet. LWR Fuel Perform.* (2004), pp. 329–338.
[23] R. Dowek, Les Gaz de Fission Dans Les Combustibles REP Irradiés : Un État Détaillé à Fort Taux de Combustion, 2021.
[24] J. Noirot, R. Dowek, I. Zacharie-aubrun, T. Blay, and M. Cabié, Ongoing Artic. (2022).
[25]ISO 13383-12012 (2012).
[26] B. Michel, I. Ramière, I. Viallard, C. Introini, M. Lainet, N. Chauvin, V. Marelle, A. Boulore, T. Helfer, R. Masson, J. Sercombe, J.C. Dumas, L. Noirot, and S. Bernaud, *Two Fuel Performance Codes of the PLEIADES Platform: ALCYONE and GERMINAL* (2020).
[27] V. Marelle, P. Goldbronn, S. Bernaud, E. Castelier, J. Julien, K. Nkonga, I. Ramiere, V. Marelle, P. Goldbronn, S. Bernaud, E. Castelier, J. Julien, V. Marelle, P. Goldbronn, S. Bernaud, E. Castelier, J. Julien, K. Nkonga, L. Noirot, and I. Ramière, in *Topfuel, Boise, Idaho (USA)* (2020).
[28] I. Zacharie-Aubrun, T. Blay, C. Ciszak, C. Cagna, and S. Chalal, NuMat, Montpellier (France) 13108 (2016).
[29] I. Zacharie-Aubrun and T. Blay, in *Topfuel, Karlsruhe (Germany)* (2016).
[30] M. Ben Saada, N. Gey, B. Beausir, X. Iltis, H. Mansour, and N. Malou, Mater. Charact. **133**, 112 (2017).
[31] F. Bachmann, R. Hielscher, and H. Schaeben, Solid State Phenom. **160**, 63 (2010).
[32] J.K. Mackenzie, Biometrika **45**, 229 (1958).
[33] F.J. Humphreys, J. Mater. Sci. **36**, 3833 (2001).
[34] T. Wiss, *Radiation Effects in UO2* (Elsevier Inc., 2012).
[35] J. Noirot, Y. Pontillon, S. Yagnik, and J.A. Turnbull, J. Nucl. Mater. **462**, 77 (2015).

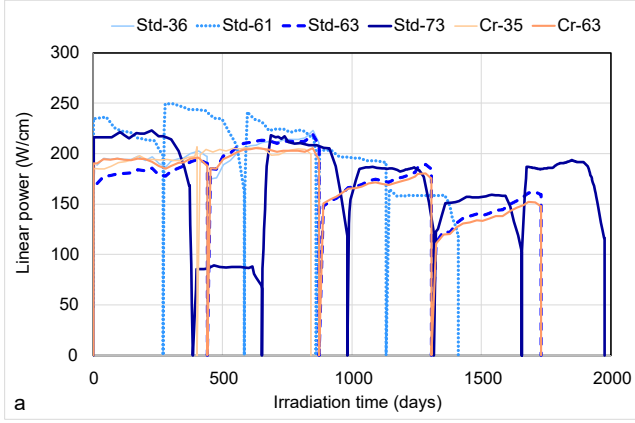
Std-36
Std-61
Std-63
Std-73
Cr-35
Cr-63
Linear power (W/cm)
300
250
200
150
100
50
0
0
500
1000
1500
2000
Irradiation time (days)
a

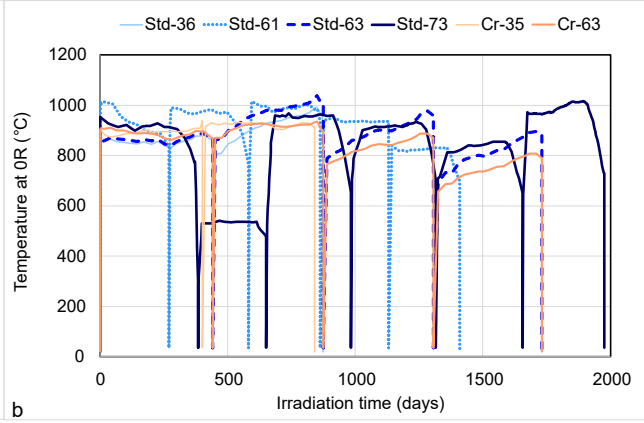
Std-36
Std-61
Std-63
Std-73
Cr-35
Cr-63
Temperature at 0R (°C)
1200
1000
800
600
400
200
0
0
500
1000
1500
2000
Irradiation time (days)
b

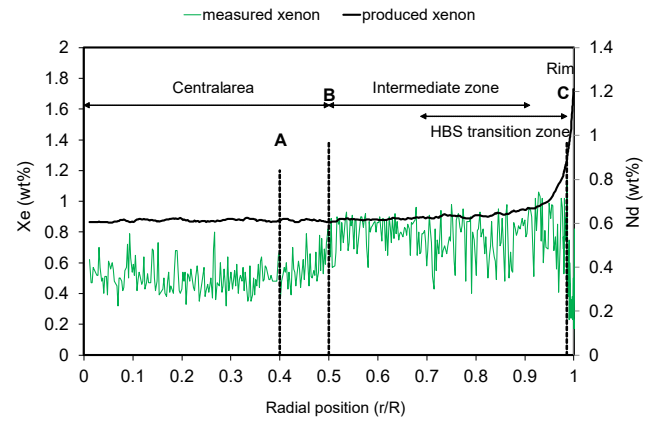
measured xenon
produced xenon
Centralarea
B
Intermediate zone
Rim
C
HBS transition zone
A
Xe (wt%)
Nd (wt%)
Radial position (r/R)
0
0.1
0.2
0.3
0.4
0.5
0.6
0.7
0.8
0.9
1
0.2
0.4
0.6
0.8
1.2
1.4
1.6
1.8
2

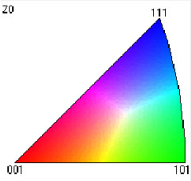
20
111
001
101

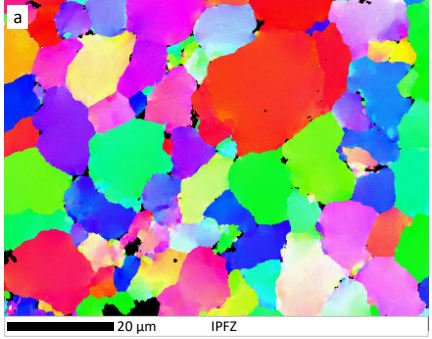
a
20 µm
IPFZ

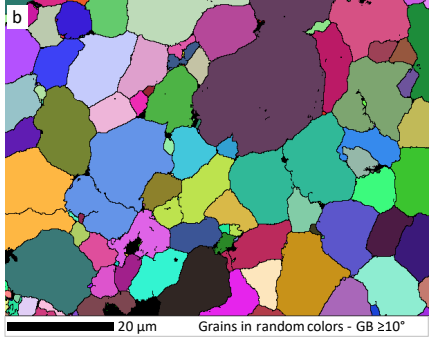
b
20 µm
Grains in random colors - GB ≥10°

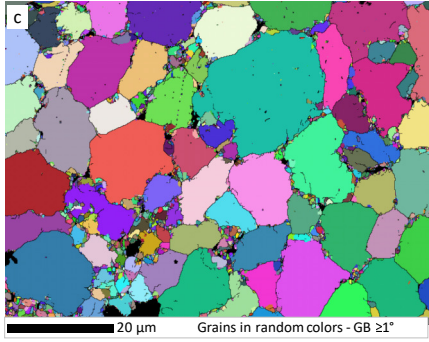
c
20 µm
Grains in random colors - GB ≥1°

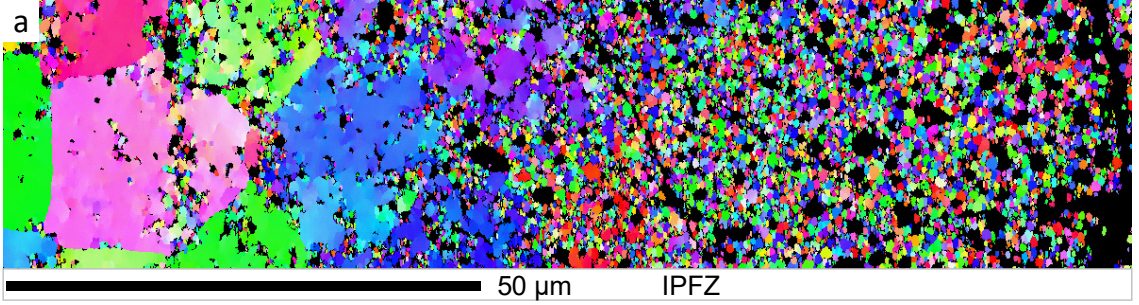
a
50 µm
IPFZ

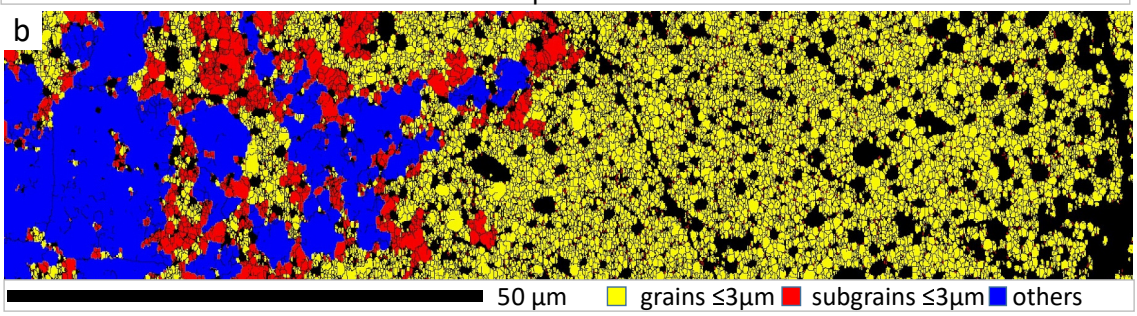
b
50 µm
grains ≤3µm
subgrains ≤3µm
others

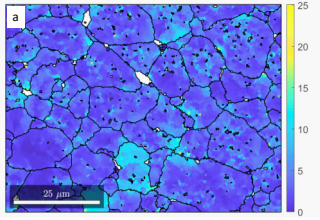
a
25 μm
25
20
15
10
5
0

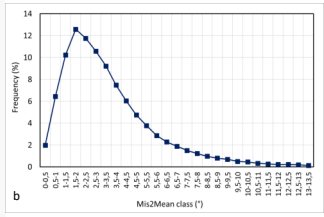
Frequency (%)
14
12
10
8
6
4
2
0
0-0.5
0.5-1
1-1.5
1.5-2
2-2.5
2.5-3
3-3.5
3.5-4
4-4.5
4.5-5
5-5.5
5.5-6
6-6.5
6.5-7
7-7.5
7.5-8
8-8.5
8.5-9
9-9.5
9.5-10
10-10.5
10.5-11
11-11.5
11.5-12
12-12.5
12.5-13
13-13.5
Mis2Mean class (°)
b

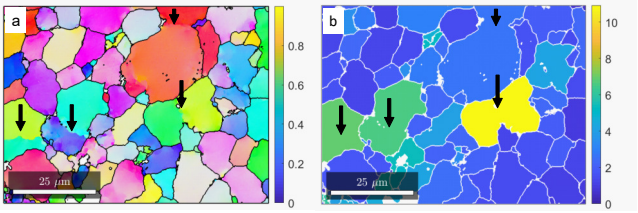
a
25 μm
0.8
0.6
0.4
0.2
0
b
25 μm
10
8
6
4
2
0

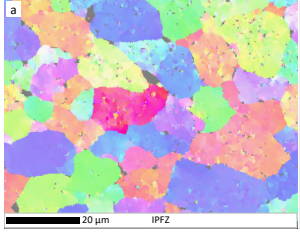
a
20 µm
IPFZ

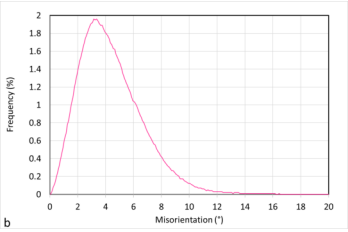
Frequency (%)
2
1.8
1.6
1.4
1.2
1
0.8
0.6
0.4
0.2
0
0
2
4
6
8
10
12
14
16
18
20
Misorientation (°)

b

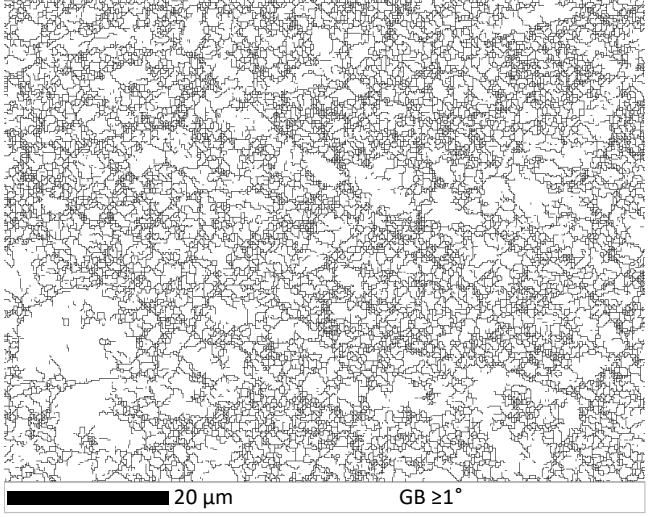
20 µm
GB ≥1°

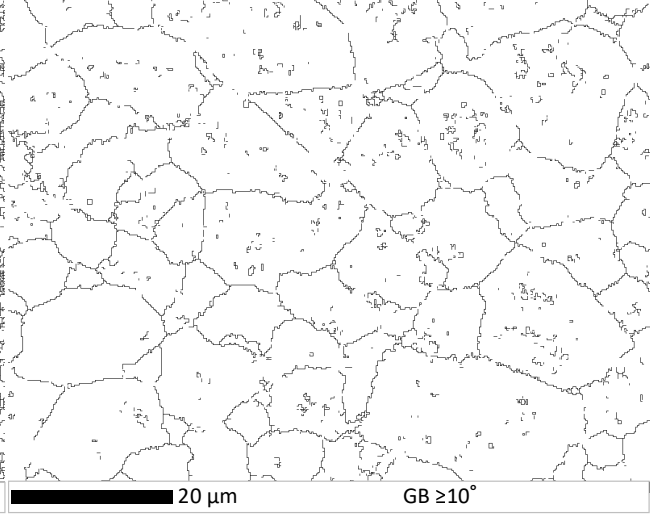
20 µm
GB ≥10°

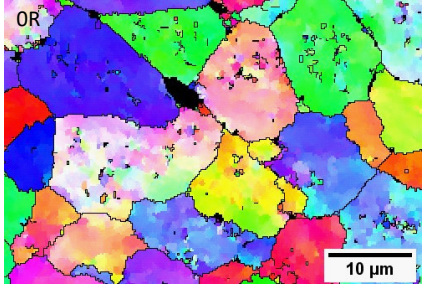
0R
10 µm

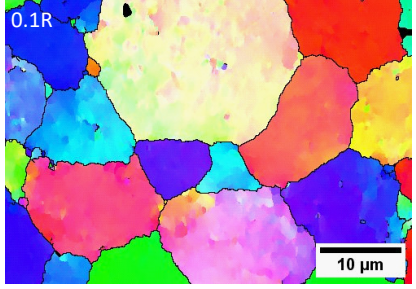
0.1R
10 µm

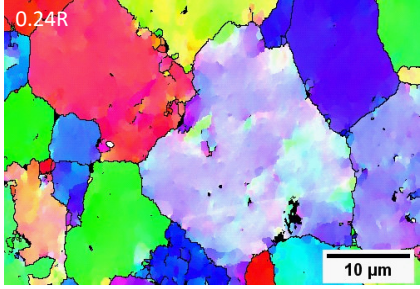
0.24R
10 µm

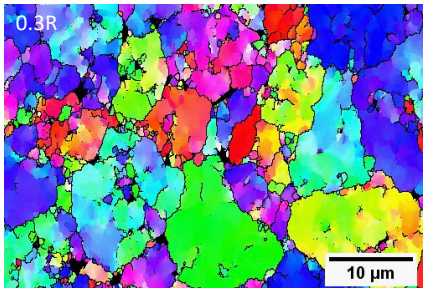
0.3R
10 µm

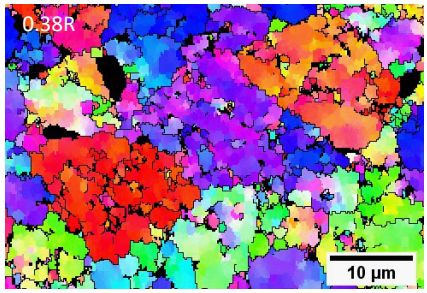
0.38R
10 µm

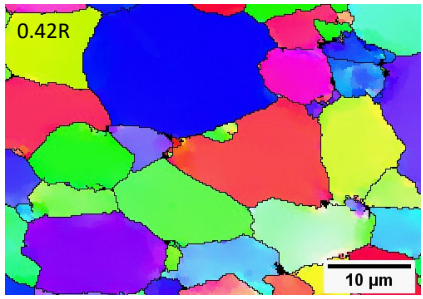
0.42R
10 µm

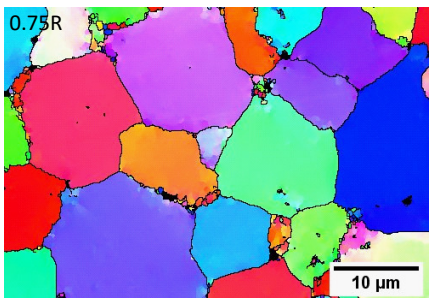
0.75R
10 µm

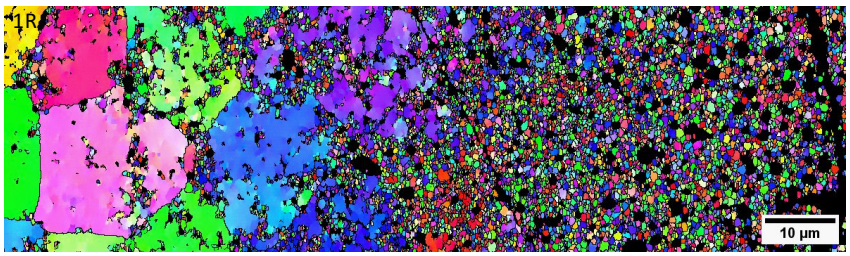
1R
10 µm

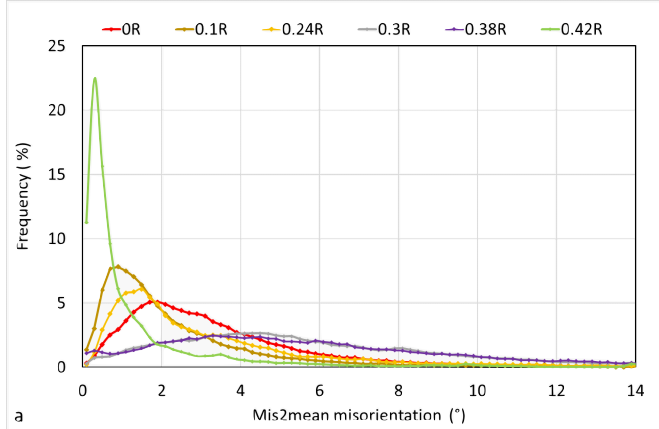
0R
0.1R
0.24R
0.3R
0.38R
0.42R
Frequency (%)
Mis2mean misorientation (°)
a

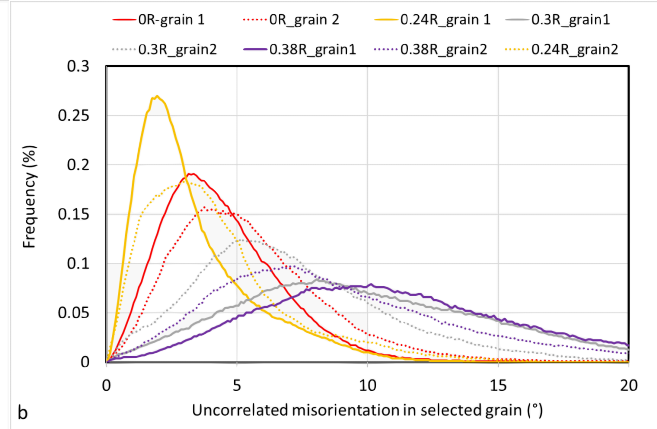
0R-grain 1
0R_grain 2
0.24R_grain 1
0.3R_grain1
0.3R_grain2
0.38R_grain1
0.38R_grain2
0.24R_grain2
Frequency (%)
Uncorrelated misorientation in selected grain (°)
b

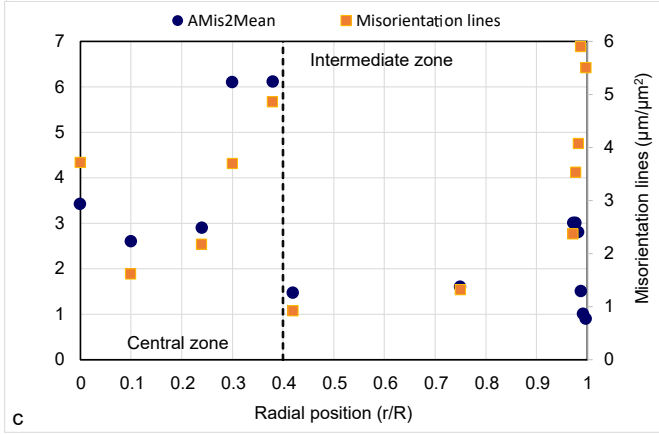
AMis2Mean
Misorientation lines
Intermediate zone
Central zone
Misorientation lines (µm/µm²)
Radial position (r/R)
c

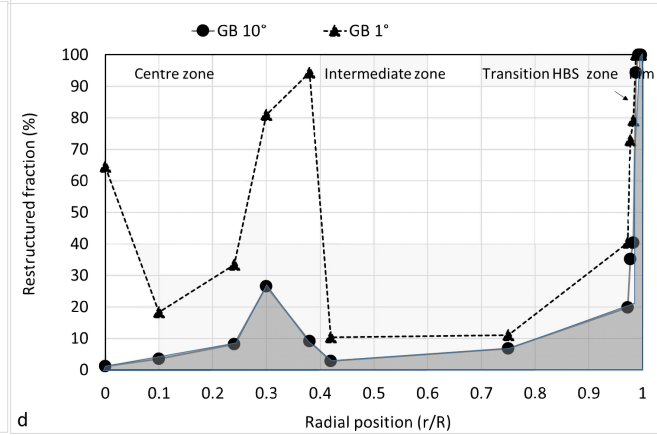
GB 10°
GB 1°
Centre zone
Intermediate zone
Transition HBS zone
Restructured fraction (%)
Radial position (r/R)
d

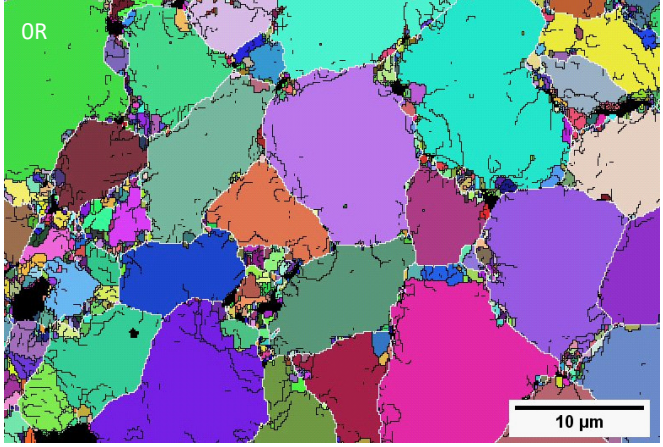
0R
10 µm

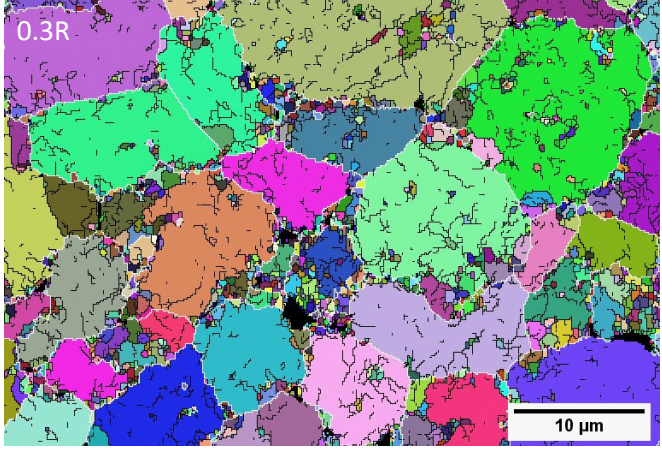
0.3R
10 µm

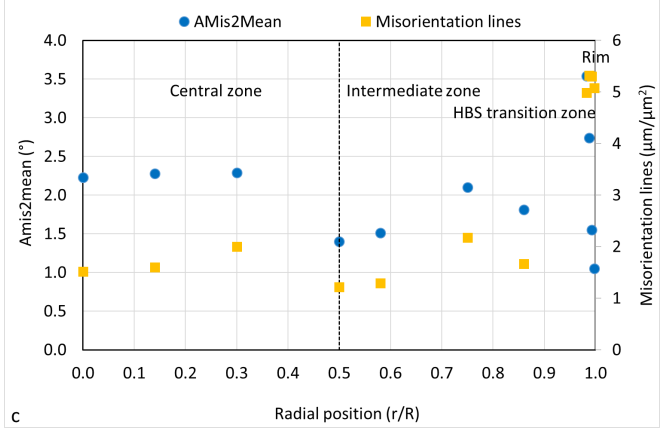
AMis2Mean
Misorientation lines
Central zone
Intermediate zone
HBS transition zone
Rim
Amis2mean (°)
Misorientation lines (µm/µm²)
Radial position (r/R)
c

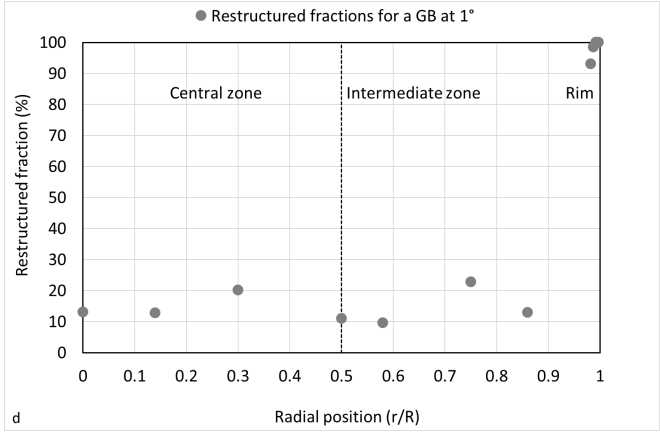
Restructured fractions for a GB at 1°
Central zone
Intermediate zone
Rim
Restructured fraction (%)
Radial position (r/R)
d

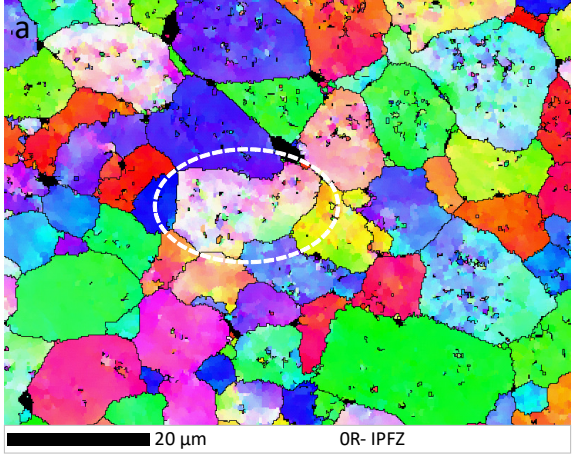
a
20 µm
0R- IPFZ

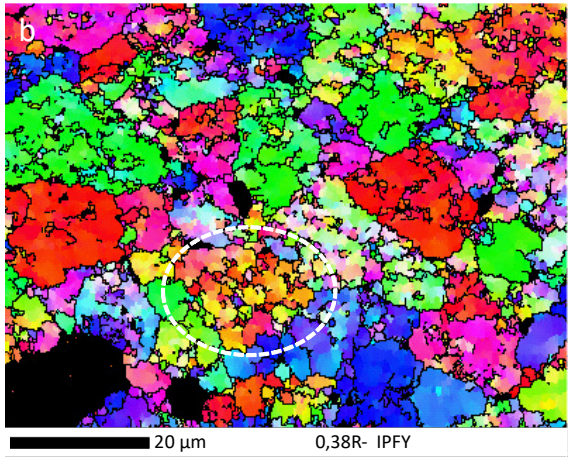
b
20 µm
0,38R- IPFY


c

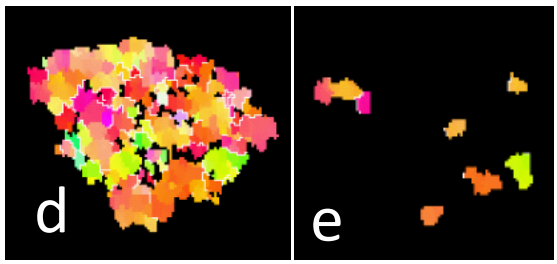
d
e

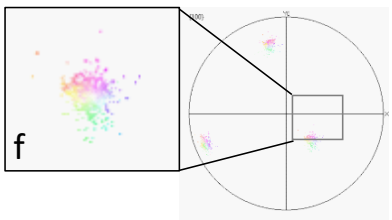
f

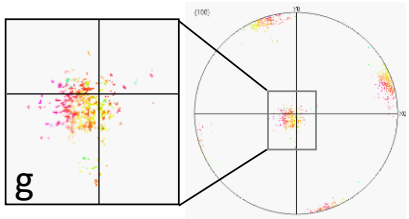
g

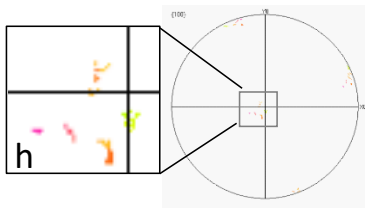
h

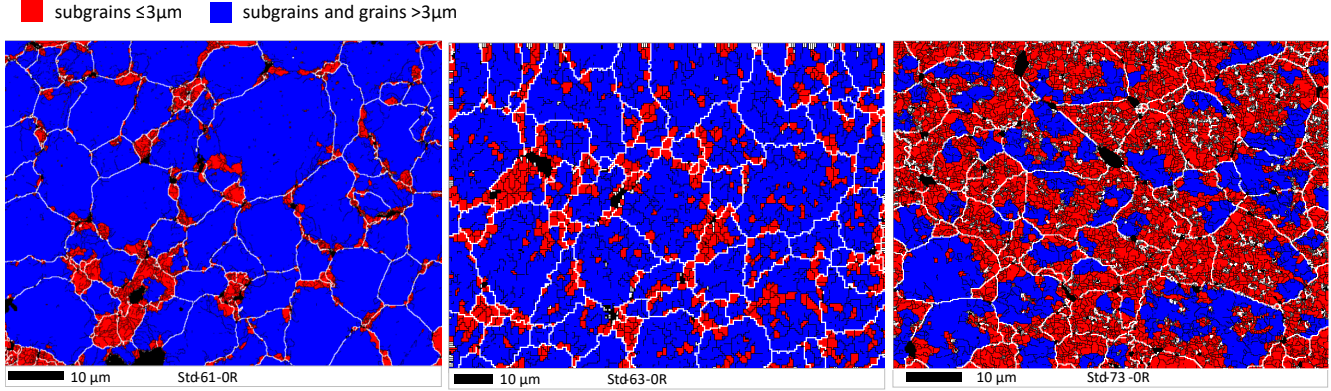
subgrains ≤3µm
subgrains and grains >3µm
10 µm
Std-61-0R
10 µm
Std-63-0R
10 µm
Std-73 -0R

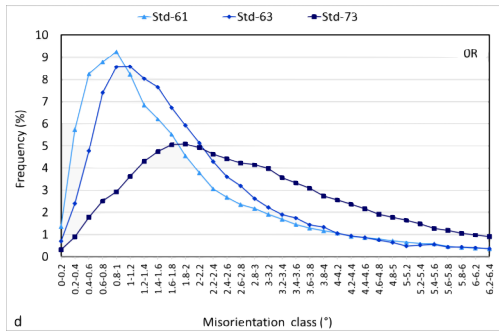
Std-61
Std-63
Std-73
0R
Frequency (%)
Misorientation class (°)
d

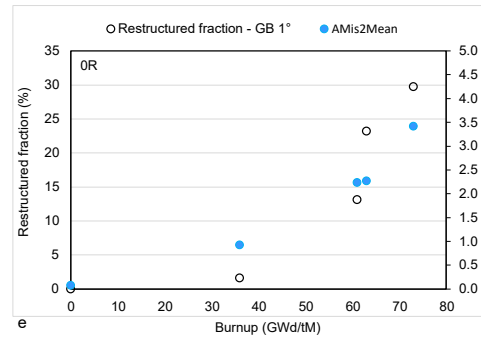
Restructured fraction - GB 1°
AMis2Mean
0R
Restructured fraction (%)
AMis2Mean (°)
Burnup (GWd/tM)
e

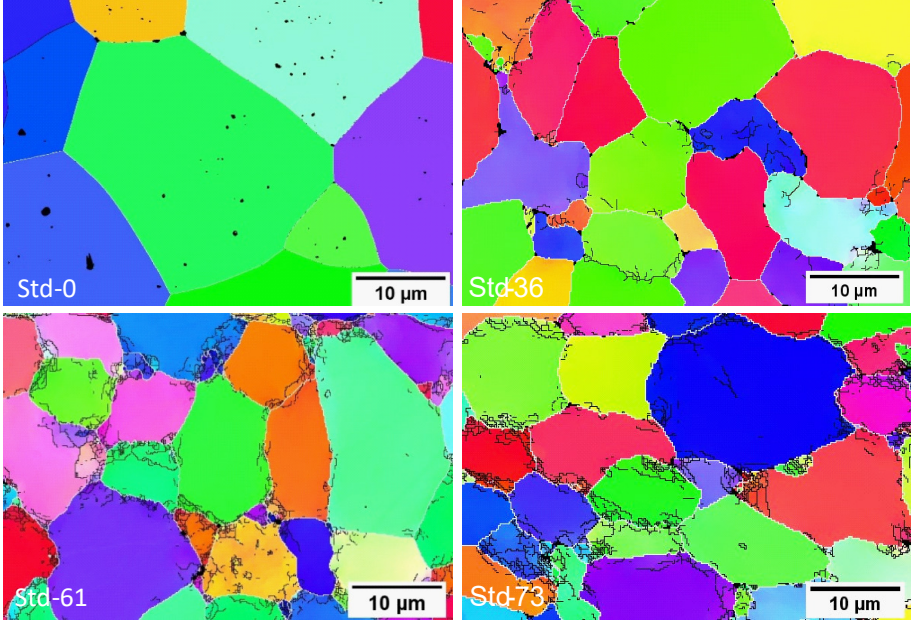
Std-0
10 µm
Std-36
10 µm
Std-61
10 µm
Std-73
10 µm

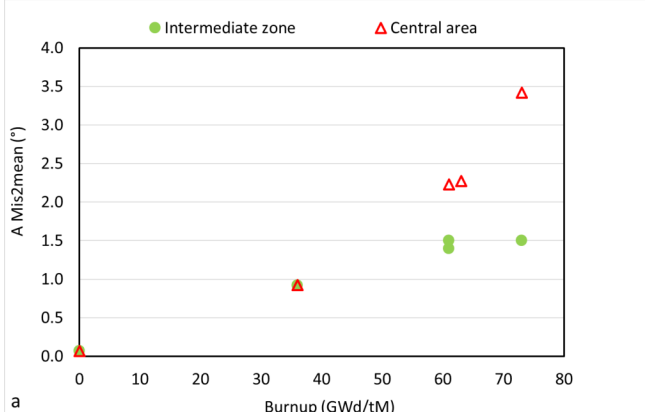
Intermediate zone
Central area
A Mis2mean (°)
Burnup (GWd/tM)
a

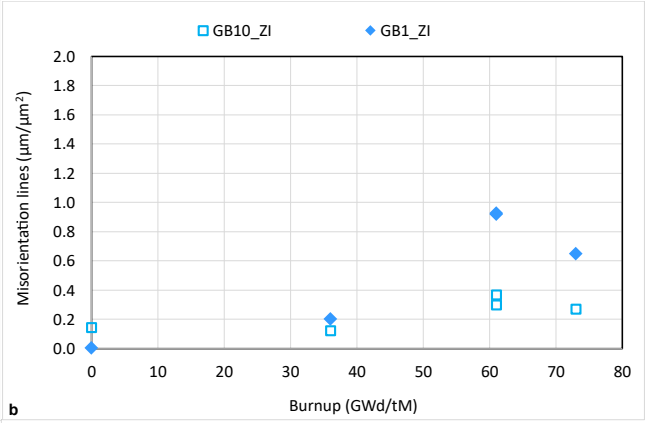
GB10_ZI
GB1_ZI
Misorientation lines (µm/µm²)
Burnup (GWd/tM)
b

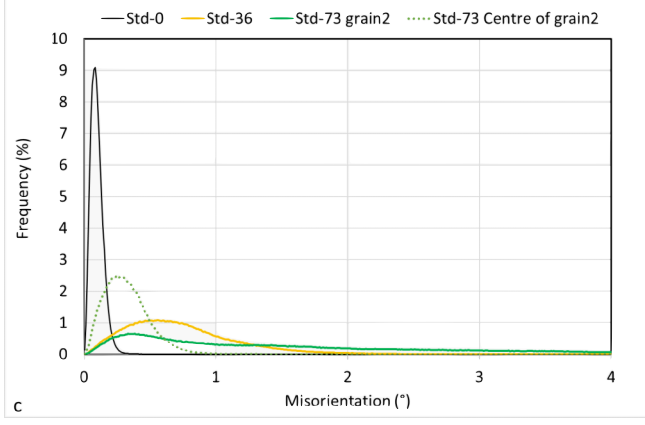
Std-0
Std-36
Std-73 grain2
Std-73 Centre of grain2
Frequency (%)
Misorientation (°)
c

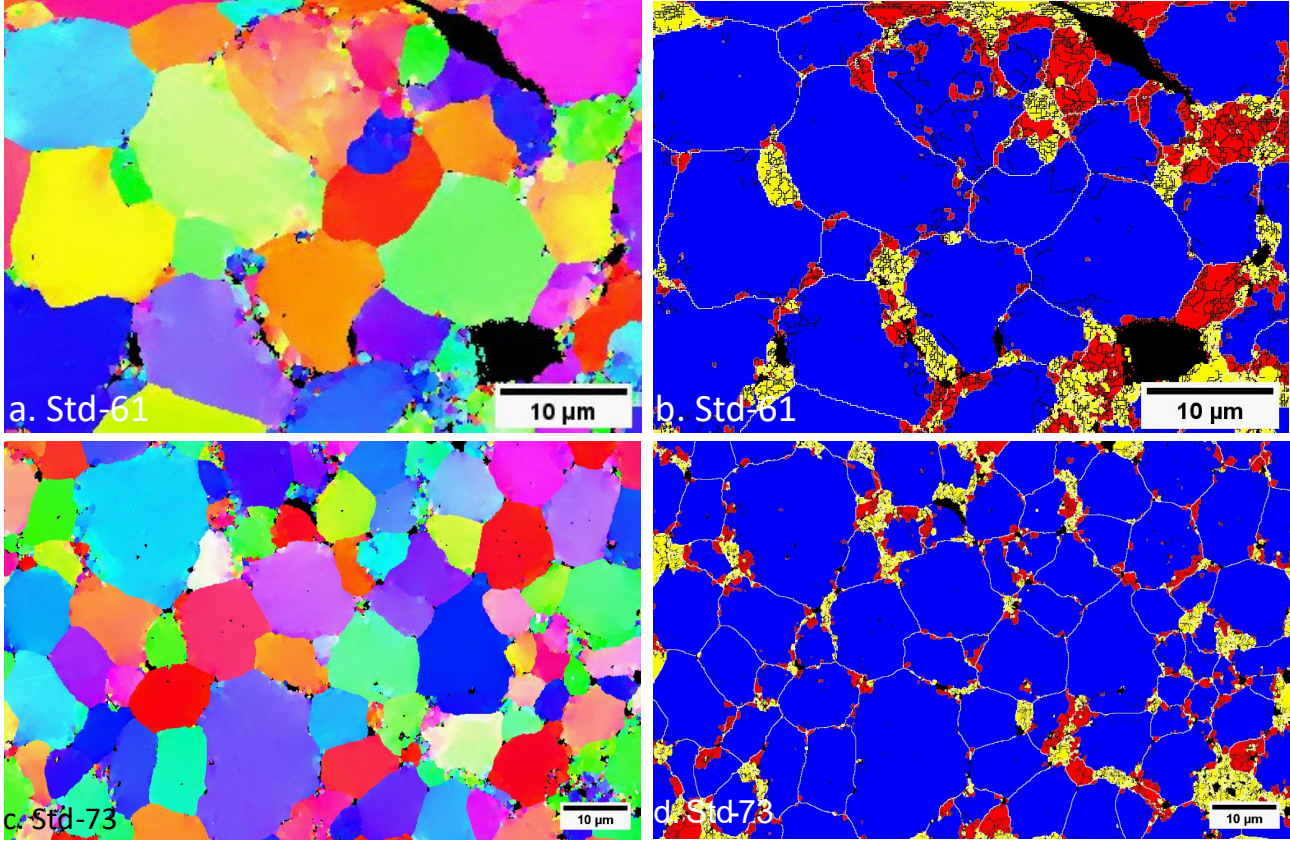
a. Std-61
10 µm
b. Std-61
10 µm
c. Std-73
10 µm
d. Std-73
10 µm

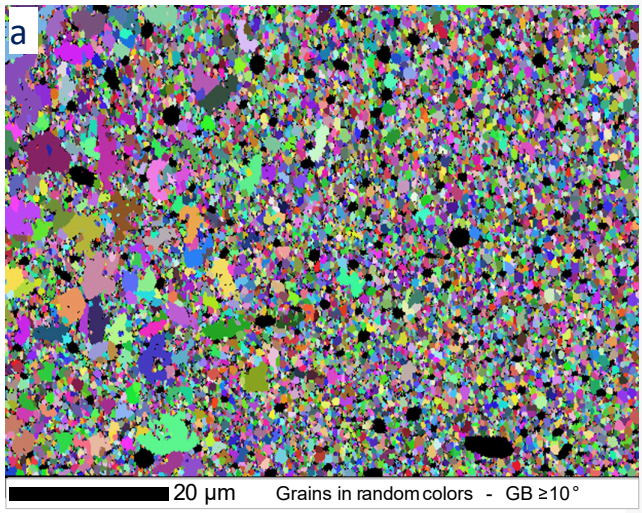
a
20 µm
Grains in random colors - GB ≥10°

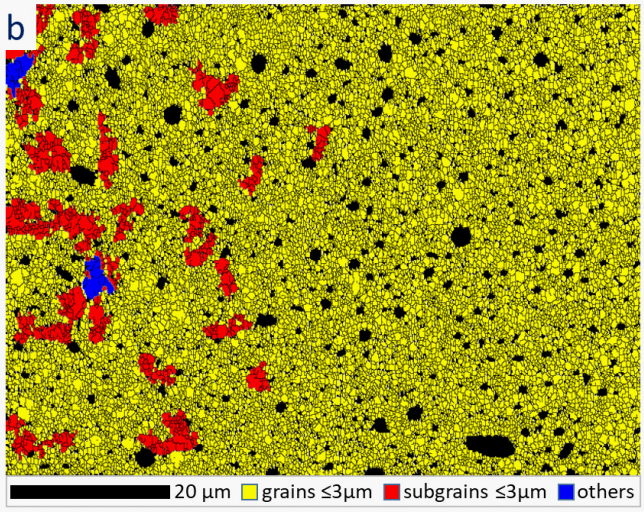
b
20 µm
grains ≤3µm
subgrains ≤3µm
others

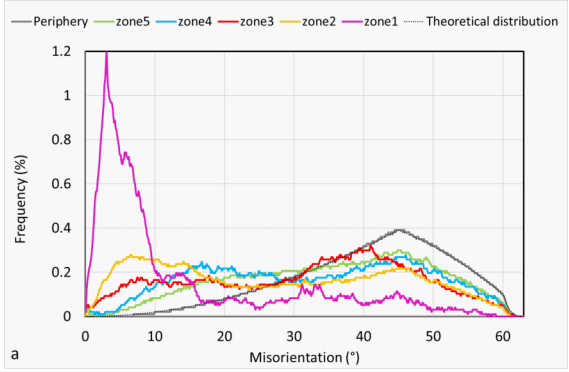
Periphery
zone5
zone4
zone3
zone2
zone1
Theoretical distribution
Frequency (%)
Misorientation (°)
a

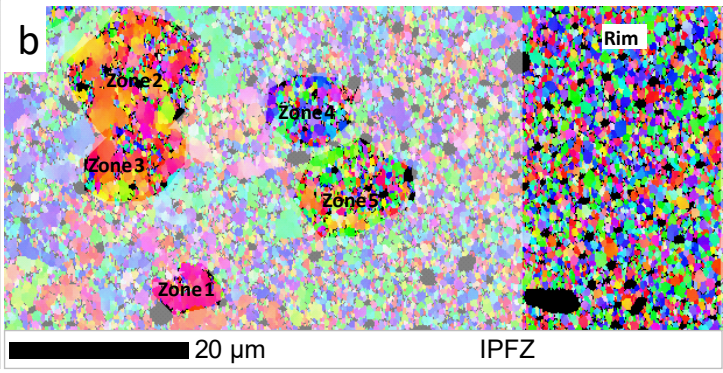
b
Zone 2
Zone 4
Zone 3
Zone 5
Zone 1
Rim
20 µm
IPFZ

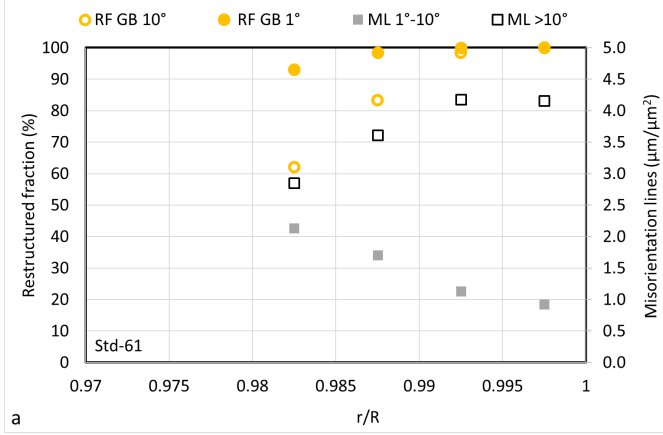
RF GB 10°
RF GB 1°
ML 1°-10°
ML >10°
Restructured fraction (%)
Misorientation lines (μm/μm²)
Std-61
r/R
a

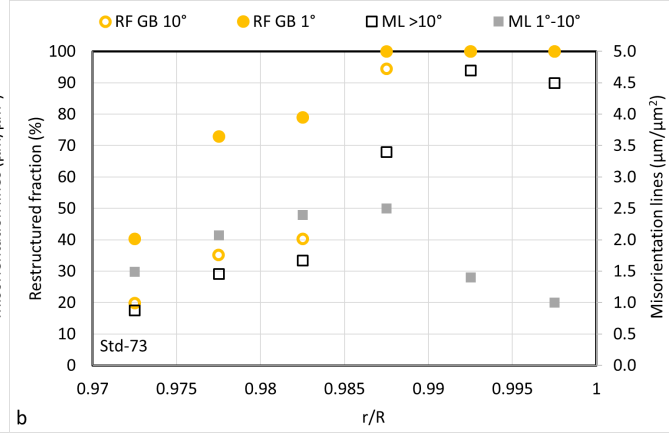
RF GB 10°
RF GB 1°
ML >10°
ML 1°-10°
Restructured fraction (%)
Misorientation lines (μm/μm²)
Std-73
r/R
b

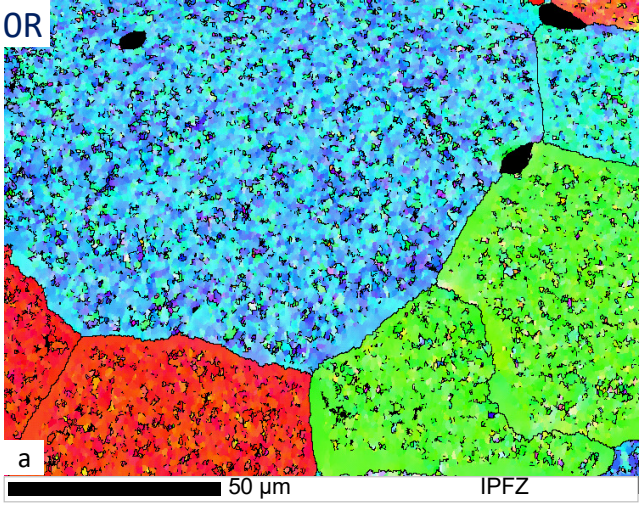
0R
a
50 µm
IPFZ

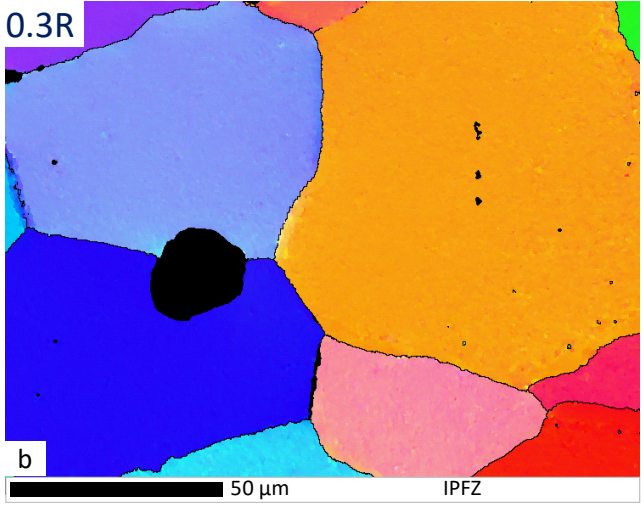
0.3R
b
50 µm
IPFZ

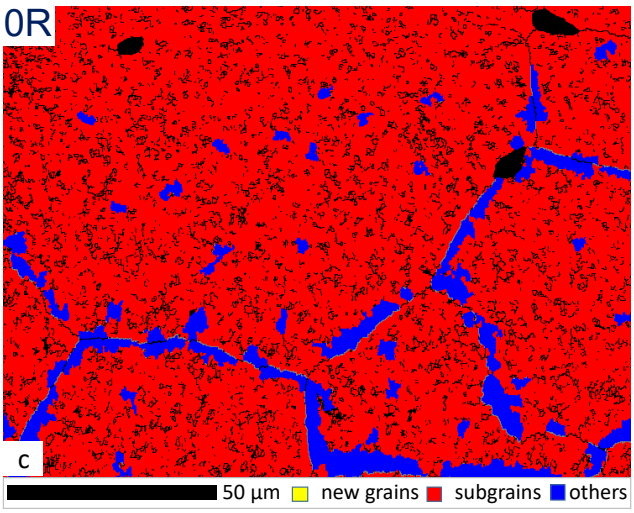
0R
c
50 µm
new grains
subgrains
others

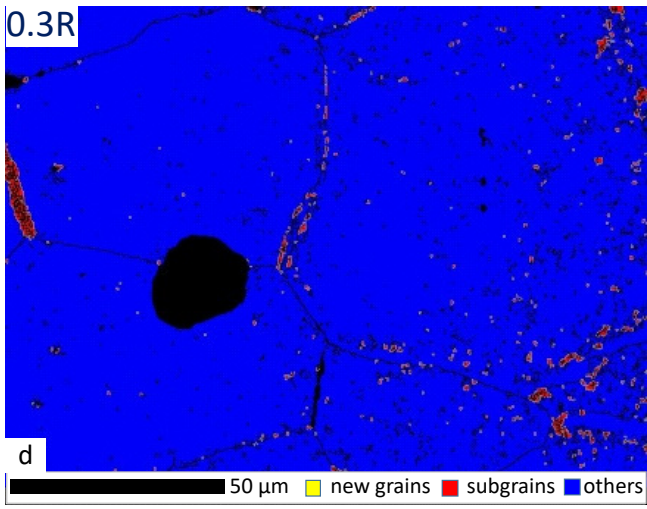
0.3R
d
50 µm
new grains
subgrains
others

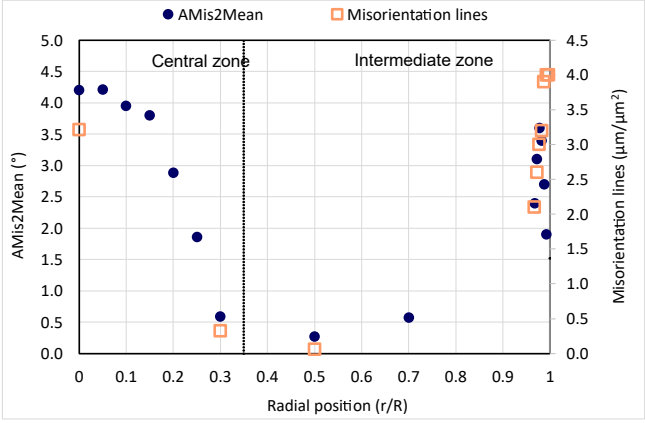
AMis2Mean
Misorientation lines
Central zone
Intermediate zone
AMis2Mean (°)
Misorientation lines (µm/µm²)
Radial position (r/R)
5.0
4.5
4.0
3.5
3.0
2.5
2.0
1.5
1.0
0.5
0.0
0
0.1
0.2
0.3
0.4
0.5
0.6
0.7
0.8
0.9
1

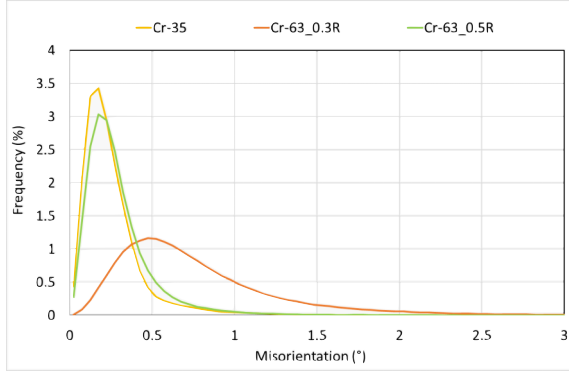
Cr-35
Cr-63_0.3R
Cr-63_0.5R
Frequency (%)
Misorientation (°)
0
0.5
1
1.5
2
2.5
3
3.5
4

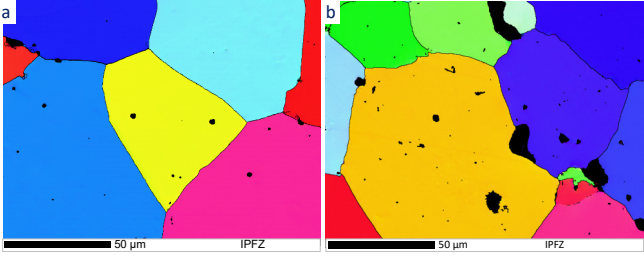
a
50 µm
IPFZ
b
50 µm
IPFZ

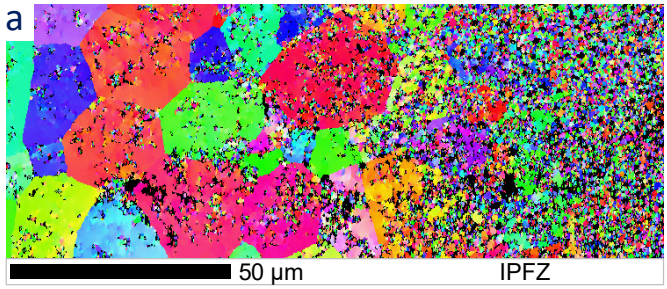
a
50 µm
IPFZ

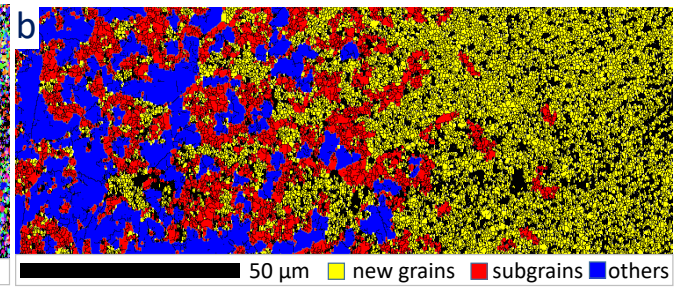
b
50 µm
new grains
subgrains
others

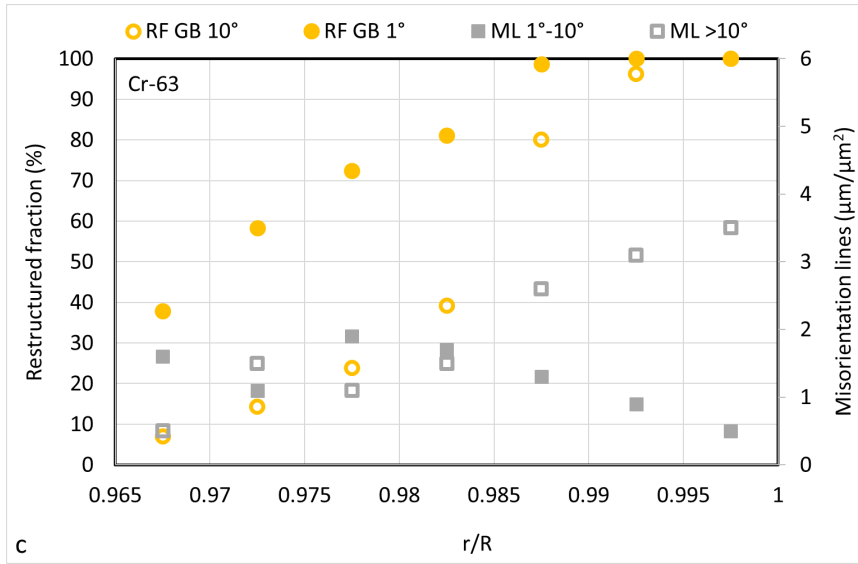
RF GB 10°
RF GB 1°
ML 1°-10°
ML >10°
Cr-63
Restructured fraction (%)
Misorientation lines (µm/µm²)
r/R
c

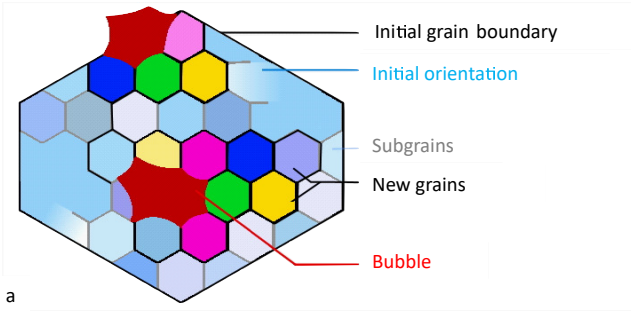
Initial grain boundary
Initial orientation
Subgrains
New grains
Bubble

a

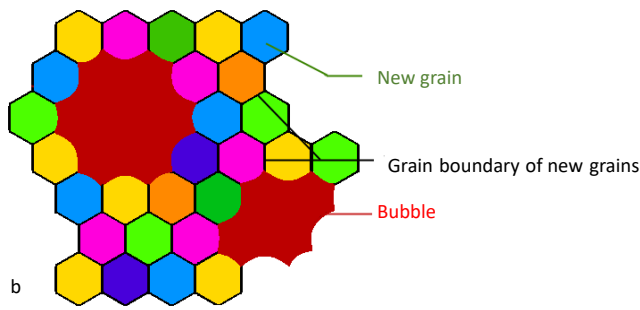
New grain
Grain boundary of new grains
Bubble

b

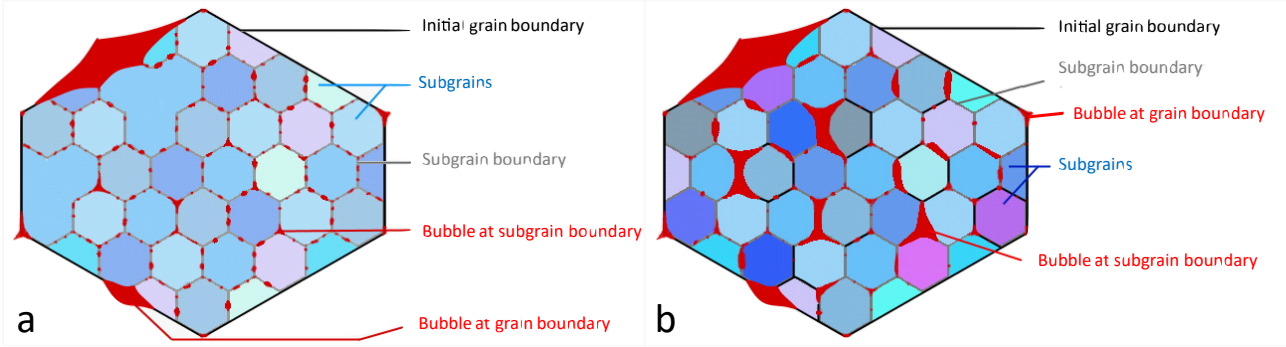
Initial grain boundary
Subgrains
Subgrain boundary
Bubble at subgrain boundary
Bubble at grain boundary
a
Initial grain boundary
Subgrain boundary
Bubble at grain boundary
Subgrains
Bubble at subgrain boundary
b